Astronomy & Astrophysics manuscript no. LG_NGC3532
June 12, 2026

Gravity-mode main-sequence pulsators in the open clusters NGC 3532 and NGC 2516

Instability strip, near-core rotation, and internal structure

Gang Li (李刚) [1,2], Chenyu He (贺辰昱) [3,4], Joey S. G. Mombarg[5], Dario J. Fritzewski[1], and Conny Aerts[1,6,7]

[1] Institute of Astronomy (IvS), Department of Physics and Astronomy, KU Leuven, Celestijnenlaan 200D, 3001 Leuven, Belgium
e-mail: gang.li@unisq.edu.au, conny.aerts@kuleuven.be
[2] Centre for Astrophysics, University of Southern Queensland, Toowoomba, QLD 4350, Australia
[3] School of Physics and Astronomy, Sun Yat-sen University, Zhuhai, 519082, People's Republic of China
[4] CSST Science Center for the Guangdong–Hong Kong–Macau Greater Bay Area, Zhuhai, 519082, People's Republic of China
[5] Université Paris-Saclay, Université de Paris, Sorbonne Paris Cité, CEA, CNRS, AIM, F-91191 Gif-sur-Yvette, France
[6] Department of Astrophysics, IMAPP, Radboud University Nijmegen, PO Box 9010, 6500 GL Nijmegen, The Netherlands
[7] Max-Planck-Institut für Astronomie, Königstuhl 17, D-69117 Heidelberg, Germany

??, ??

ABSTRACT

Context. Studying pulsating stars in clusters opens a new window onto stellar physics. More specifically, gravity-mode (g-mode) pulsators in open clusters allow us to measure their near-core rotation rates. Combined with the rough cluster-provided age and mass constraints, these members enable an efficient test of angular momentum transport models inside stars for masses above $\sim 1.5\,M_\odot$.
Aims. Our goal is to detect g-mode pulsations in the member stars of the young open cluster NGC 3532 (~ 300 Myr), and to measure their near-core rotation rates and internal properties.
Methods. We used photometric data from the Transiting Exoplanet Survey Satellite (TESS) to extract the light curves of member stars in NGC 3532. The observed g-mode period spacings allow us to measure their near-core rotation rates and asymptotic period spacing Π_0. We further fitted isochrones to the observed colour-magnitude diagrams (CMDs) of both clusters to tighten the cluster age and to obtain stellar masses.
Results. We constrain the observed instability region occupied by the young γ Doradus member stars from a blue edge at ~ 7760 K to a red edge at ~ 7070 K, while some g-mode pulsators with higher temperatures are also seen. Our results for the near-core rotation rates show a rotation – mass relation similar to that observed in NGC 2516: for stellar masses below $1.6\,M_\odot$, the near-core rotation rate increases with increasing mass, whereas above $1.6\,M_\odot$ the stars in NGC 3532 reach a plateau, all rotating at approximately $2.8\,d^{-1}$. This mass indicates a threshold separating different rotational spin-down mechanisms in stars. We examined existing stellar evolutionary models that include angular momentum (AM) transport and found that the g-mode pulsators must have been born with an initial rotation rate above 55% of the critical value. Our simplified models, which assume spherical symmetry, AM conservation, and rigid internal rotation, suggest that either mass-dependent initial rotation rates are required to explain the observations, or that a minor AM loss is still operating for masses above $1.6\,M_\odot$. Finally, our measurements of Π_0 reveal a discrepancy with theoretical predictions for some of the pulsators, which was also found in NGC 2516, a cluster that is only about one third as old.

Key words. Asteroseismology – Stars: early-type – Stars: interiors – Stars: oscillations – Stars: rotation – open clusters and associations: individual: NGC 3532 and NGC 2516

1. Introduction

Although it is well known that mass and chemical composition are the two most important parameters determining a star's evolutionary track (e.g. Kippenhahn & Weigert 1990), many physical processes remain poorly understood. This is particularly the case for internal rotation and its various influences on transport processes, which keep challenging our knowledge of stellar physics (e.g. Maeder 2009). For early-type main-sequence stars (with effective temperatures $T_{\rm eff} \gtrsim 6500$ K), both spectroscopic observations (e.g., $v \sin i$ measurements or polarimetry; Royer et al. 2007; Zhao et al. 2009; Che et al. 2011; Bouchaud et al. 2020) and photometric observations (e.g., of pulsations or surface modulations; Van Reeth et al. 2016; Li et al. 2020a) show that their rotation is much faster than the one of cool main-sequence stars. Large samples of galactic stars of spectral types B, A, or F (with $M \gtrsim 1.5\,M_\odot$) show them to cover rotation rates from zero to almost the critical rate. The majority among these stars reaches rotation velocities between 20% and 40% of the critical Keplerian value (Zorec & Royer 2012; Dufton et al. 2013; Sun et al. 2021; Aerts 2025). Some B-type stars (namely Be stars) can reach as high as ~90% of the critical velocity (Townsend et al. 2004; Bastian et al. 2017; Hastings et al. 2020). Statistical samples for BAF-type stars with measurements of their internal rotation within clusters are much smaller. Yet some AF-type stars were found to rotate at up to ~50% of the critical velocity in the young open cluster NGC 2516 (Li et al. 2024a).

The effects of rapid rotation profoundly reshape the evolution of early-type stars. The centrifugal force makes a star oblate, thereby altering its internal structure. Treating rapid rotation in stellar models is not an easy task, as it is intrinsically a two-dimensional problem. Researchers either pursue the development of 2D stellar codes (e.g., ESTER; Espinosa Lara & Rieutord 2013; Rieutord et al. 2016; Reese et al. 2021; Mombarg et al. 2023, 2024c) or apply corrections to existing 1D models (e.g., the shellular approximation; Meynet & Maeder 1997; Paxton et al. 2013). In addition, rotational shear drives the transport of AM and induces element mixing through hydrodynamical instabilities (Heger et al. 2000, 2005). The extra fuel supplied to the stellar core significantly prolongs a star's lifetime, introducing uncertainties in age determinations from stellar models with different input physics.

The effects of rotation on the structure and lifetime of early-type stars have been proposed to explain the widely observed extended main sequences in Galactic and Magellanic Cloud star clusters younger than 2 Gyr (e.g. Bastian & de Mink 2009; Li et al. 2014; D'Antona et al. 2015; Milone et al. 2018; Cordoni et al. 2018). This scenario has been supported by both stellar-population modelling that incorporates rotational effects (e.g. D'Antona et al. 2015) and spectroscopic measurements of projected rotation rates (e.g. Marino et al. 2018a,b; Sun et al. 2019a,b; Kamann et al. 2020, 2023). However, existing observational evidence is largely limited to stellar surfaces. An appreciable lack of observational calibration remains for internal rotation and its impact on stellar structure and internal material transport — which is the key underlying physics. Therefore, it is necessary to investigate the impact of rotation on stellar evolution from another perspective than often done — that of the stellar interior in addition to the stellar surface.

Asteroseismology, the study of stellar internal oscillations, has become an effective means of probing and calibrating stellar internal physics (Aerts et al. 2010; Aerts 2021). For over a decade, gravity modes (g modes hereafter) in early-type main-sequence stars have been used to reveal near-core rotation rates (Van Reeth et al. 2015c, 2016; Li et al. 2020b,a; Garcia et al. 2022b), based on the fact that their mode overtones (with the same angular degree l and azimuthal order m, but increasing radial order n_g) are modified by rotation (Lee & Saio 1997; Townsend 2003; Saio et al. 2018a). This effect has been clearly observed using light curves from the *Kepler* and TESS (Transiting Exoplanet Survey Satellite) missions (Borucki et al. 2010; Ricker et al. 2015).

However, to calibrate the process of AM transport, it is not sufficient to measure only the internal rotation rates. It is also required to deduce the evolution of the internal rotation profiles as stars age, along with the change in their radius. Deriving stellar ages is not straightforward, so previous studies on field stars have had to rely on some age indicators. A simple age indicator is the surface gravity $\log g$ (e.g. Fig. 6 in Aerts 2021), but $\log g$ suffers from large uncertainties and parameter degeneracies. For main-sequence stars, the central hydrogen abundance X_c (e.g. Mombarg et al. 2021, 2024a) or the asymptotic g-mode period spacing Π_0 (e.g. Miglio et al. 2008; Bouabid et al. 2013; Ouazzani et al. 2019; Pedersen 2022; Moyano et al. 2023) can be used as age diagnostics, but both are model-dependent. For post-main-sequence stars, the mixed-mode density (i.e. the number of gravity modes per pressure-mode frequency range; Gehan et al. 2018, Li et al. 2024b) is often applied to trace age beyond the terminal-age main sequence. Direct measurements linking stellar internal rotation rates to age are still lacking.

We therefore turn our attention to the member stars in open clusters. Stars in an open cluster are born from the same molecular cloud. Moreover, the timescales of star formation in star clusters are thought to be much shorter than most clusters' ages since the strong feedback from the massive stars expels most remaining gas from the cluster in short time in order of 10^5 years (Bastian & Goodwin 2006; Longmore et al. 2014). Therefore, stars in an open cluster are generally thought to share the same age, chemical composition, and distance (Lada & Lada 2003; Salaris & Cassisi 2005), although there are exceptions, as some clusters exhibit extended tidal tails or large halos (e.g. Meingast & Alves 2019; Bouma et al. 2021). Isochrone fitting, which relies on stellar evolution models with a specific set of input physics (e.g., MIST; Dotter 2016; Choi et al. 2016, or PARSEC; Nguyen et al. 2022, 2025), is widely used to determine the ages of clusters and the global parameters of their member stars (Kharchenko et al. 2013; Bossini et al. 2019; Cantat-Gaudin et al. 2018, 2020; Hunt & Reffert 2024; Reyes et al. 2024). The information and constraints provided by clusters offer valuable support to asteroseismic studies, such as tracing the evolution of convective envelopes in the stars of M 67 (Reyes et al. 2025), measuring the age of NGC 6866 using solar-like oscillators on the red giant branch (Brogaard et al. 2023), and the first attempt at age-dating using main-sequence g-mode pulsators in UBC 1 (Fritzewski et al. 2024). In recent years, numerous studies have combined open clusters with asteroseismology. Here we highlight some representative examples (Corsaro et al. 2012; Balona et al. 2013; Miglio et al. 2016; Stello et al. 2016b; Murphy et al. 2021; Tailo et al. 2022; Bedding et al. 2023; Murphy et al. 2022; Li et al. 2024a; Murphy et al. 2024; Tayar & Joyce 2025; Mankowski et al. 2025; Berry et al. 2025; Mani et al. 2025).

Previous asteroseismic studies of stars in clusters have typically focused on a single cluster. To investigate the evolution of stellar rotation as a function of age, we extend our seismic analysis from one cluster to two similar clusters. This is part of a long-term project to build up a comprehensive asteroseismic understanding of open clusters having a range of ages. As an initial comparative step, we combine NGC 2516 ($\sim$ 130 Myr) and NGC 3532 ($\sim$ 300 Myr) because they exhibit similar rotational properties. We have recently conducted pilot studies on NGC 2516: observational analyses revealed that many member stars are rotating at approximately 50% of their critical rotation rates, as inferred from their g-mode pulsations (Li et al. 2024a). Subsequently, we performed detailed asteroseismic modelling and determined an asteroseismic age for NGC 2516 of 132 ± 8 Myr (Li et al. 2025).

In this paper, we outline how intermediate-mass g-mode pulsators and low-mass rotational variables spin down from $\sim$ 130 Myr to $\sim$ 300 Myr from novel asteroseismology and literature gyrochronology, respectively (Li et al. 2024a, 2025; Fritzewski et al. 2020, 2021a) in these two clusters. We test current stellar evolutionary models that include asteroseismology-calibrated AM transport. This paper is organised as follows. In Sect. 2, we summarise previous literature results on the age, extinction, and metallicity of NGC 3532. Sect. 3 presents the data reduction, including membership identification, TESS photometry, and the evaluation of contamination levels. After deriving the near-core rotation rates of the member stars, we conducted isochrone fittings to the observed colour–magnitude diagrams (CMDs) of the two clusters to obtain the masses of the seismic targets, as described in Sect. 4. In Sect. 5, we report our asteroseismic results, including the observed γ Dor instability strip with age younger than $\sim$ 300 Myr, the dependence of near-core rotation rates on stellar mass, and the tension between Π_0 and

stellar mass. We also examine AM transport in stellar evolutionary models in Sect. 5. We first test the existing stellar evolution grid by Mombarg et al. (2024a), and then test an alternative AM transport model guided by the observations. Finally, our conclusions are delivered in Sect. 6.

2. The open cluster NGC 3532

NGC 3532 ($\alpha = 166°.417$, $\delta = -58°.707$; Cantat-Gaudin et al. 2020) is a rich open cluster (with thousands of member stars), of intermediate age (∼300 Myr), and with a near-solar metallicity. Comprehensive reviews of this cluster have been provided in a series of papers (Fritzewski et al. 2019, 2021b,a). He et al. (2025) provided spectroscopic study of this cluster, and Berry et al. (2025) reported 79 pressure-mode main-sequence pulsators. Here, we briefly summarise the measurements of its age, extinction, and metallicity from previous studies.

The age of NGC 3532 was estimated long ago, but with large deviations owing to the limited development of stellar modelling in the early era (Koelbloed 1959; Fernandez & Salgado 1980; Johansson 1981). Eggen (1981) reported an age of 350 Myr, which is close to modern values. Clem et al. (2011) derived an age of ∼300 Myr by fitting both the turn-off and the white dwarf sequence, and Mowlavi et al. (2012) confirmed the age of ∼300 Myr using the Geneva code (Schaller et al. 1992). The cooling sequence of cluster white dwarfs provides an independent estimate of 300 ± 25 Myr (Dobbie et al. 2012). Fritzewski et al. (2019) also reported an age of ∼300 Myr from comparison of multiple isochrone models. However, some research still gives somewhat discrepant results (340 Myr by He et al. 2025, 398 Myr by Cantat-Gaudin et al. 2020, or 238 Myr by Hunt & Reffert 2024).

The extinction or reddening of NGC 3532 has been determined several times in the literature, but with considerable scatter in the early works. More recent studies are consistent, with Clem et al. (2011) measuring $E(B-V) = 0.028 \pm 0.006$, and Fritzewski et al. (2019) obtaining $E(B-V) = 0.034 \pm 0.012$. He et al. (2025) reported an extinction of $A_V = 0.09$ mag, corresponding to $E(B-V) = 0.029$, and concluded that differential reddening across the cluster is negligible. The similar result was also reported by the Gaia-ESO survey (Jackson et al. 2022). The extinction of NGC 3532 is significantly lower than the median value found for nearby open clusters (Qin et al. 2023) despite being located 500 pc away.

NGC 3532 has a near-solar metallicity, with 1σ uncertainties that encompass the solar value. Previous studies of the cluster metallicity have mainly focused on giant stars, either photometrically (Claria & Lapasset 1988; Claria & Minniti 1988; Piatti et al. 1995; Twarog et al. 1997; Gratton 2000) or spectroscopically (Luck 1994; Gratton 2000; Netopil 2017; Cayrel de Strobel et al. 2001; Santos et al. 2012). More recent spectroscopic analyses of dwarf stars in NGC 3532 have also revealed a near-solar metallicity (Netopil et al. 2016; Fritzewski et al. 2019; Magrini et al. 2023).

3. Data reduction

3.1. Membership and sample selection

Similar to He et al. (2025), we adopted the membership identification results from Pang et al. (2022). The steps of membership determination of Pang et al. (2022) are summarised as follows. A pre-selection of targets from the *Gaia* EDR3 database (Gaia Collaboration et al. 2021) was performed using a spherical spatial cut and a proper-motion cut around the cluster coordinates, where the selected stars were required to have parallax and photometric uncertainties below 10% (Lindegren et al. 2018). The unsupervised machine-learning algorithm `StarGO` (Yuan et al. 2018) was then applied to identify cluster members based on their positions and proper motions. Finally, PARSEC v1.2S isochrones (Bressan et al. 2012; Chen et al. 2015) were fitted to further refine the membership, and stars located below the best-fitting isochrone were discarded.

As a result, NGC 3532 is the most massive open cluster in the sample of Pang et al. (2022), with a total mass of 2210 $M_\odot$. It shows a dense core and a halo-like outer structure, although the apparent halo may be affected by the high field-star density in its Galactic plane region.

We focused on stars with effective temperatures $T_{\rm eff} \gtrsim 6500$ K. These stars are expected to be classical pulsators. Among A- to F-type main-sequence stars, they can either be δ Scuti stars pulsating in pressure (p) modes (Goupil et al. 2005; Handler 2009), or γ Doradus stars pulsating in gravity (g) modes (Balona et al. 1994; Kaye et al. 1999; Van Reeth et al. 2015c). For B-type main-sequence stars, we can find slowly pulsating B-type (SPB) stars exhibiting g modes (Waelkens 1991; De Cat & Aerts 2002), and β Cephei stars exhibiting p modes (Sterken & Jerzykiewicz 1993; Aerts & De Cat 2003). In this work, we focus on the g-mode pulsators. Since there are still many pulsators found located between the instability strips of γ Dor and SPB stars (Mowlavi et al. 2013; Aerts et al. 2023), we cannot define an observational border between these two types of pulsators. Therefore, we simply refer to them collectively as g-mode pulsators without further distinction.

The criterion $T_{\rm eff} \gtrsim 6500$ K is easy to identify visually on the observed CMD. This temperature corresponds to a kink on the main sequence, where its slope changes noticeably. The hotter part of the main sequence typically exhibits a smaller slope, while the cooler part becomes slightly steeper. Therefore, we adopted a magnitude cut of $m_{\rm G} < 12$ mag, which ensures high photometric quality and selects the early-type stars of interest.

3.2. TESS photometry and g-mode signal extraction

NGC 3532 has been monitored multiple times by the TESS mission. The cluster was covered in Sectors 10 and 11 (April–May 2019), Sector 37 (April 2021), and Sectors 63–64 (March–April 2023). In addition, it was observed in Sector 90 (March 2025) and during the two consecutive sectors Sectors 99 and 100 (January–February 2026). Later, the cluster will be revisited for three consecutive sectors, Sectors 111–113 (December 2026 to February 2027), offering an uninterrupted observing window of about three months. For this work, we collected all the TESS data until Sector 90.

The TESS photometry pipeline is now mature and has been successfully applied in multiple asteroseismic studies (Garcia et al. 2022b,a; Li et al. 2024a; Fritzewski et al. 2024, 2025). We briefly summarise the procedure here. We downloaded 20×20 pixel cutouts from the TESS full-frame images (FFIs) using the `TESSCut` API (Brasseur et al. 2019). The Python package `tessutils2` (Garcia et al. 2022b)[1] was then used to perform a custom, optimised aperture photometry on the cutouts. This pipeline can reduce the systematic uncertainties and background contamination of the FFI data significantly, and can remove

[1] `https://github.com/IvS-Asteroseismology/tessutils`

long-term trends through principal component analysis (PCA) and a high-pass filter.

After obtaining the light curves, we calculated Lomb–Scargle periodograms (Lomb 1976; Scargle 1982) and extracted the pulsation frequencies using the iterative prewhitening procedure introduced by Li et al. (2019a). The extracted frequencies will be used to identify g-mode period-spacing patterns. For gravity modes, rapid rotation is unlikely to produce rotational splittings, because zonal and retrograde modes are confined to the equator, leading to strong geometric cancellation (Saio et al. 2018a). Instead, we observe a series of prograde g modes with the same l and m (most commonly $l = 1$, $m = 1$), but with increasing n. The period spacing, defined as the difference between two consecutive periods, $\Delta P = P_{n+1} - P_n$, shows a quasi-linear decreasing trend with period (Bouabid et al. 2013; Ouazzani et al. 2017). Following Van Reeth et al. (2015a), methodology for searching such period-spacing patterns was developed by Li et al. (2019a), and has since been applied to detect patterns in hundreds of γ Dor stars (Li et al. 2019b, 2020b; Yang et al. 2021; Li et al. 2024a). We adopt the same methodology here to search for period-spacing patterns in NGC 3532.

In the search for period-spacing patterns, we used data from Sectors 63 and 64 only. There are several reasons for this choice. First, the 54-day dataset provides a frequency resolution of $\delta f = 1/T \approx 0.018\,\mathrm{d}^{-1}$, corresponding to a period resolution of $\delta P = P^2 \delta f \approx 400\,\mathrm{s}$ at $P = 0.5\,\mathrm{d}$ and $\delta P \approx 100\,\mathrm{s}$ at $P = 0.25\,\mathrm{d}$. Although this resolution is not ideal for g-mode pulsators, it is sufficient to resolve period-spacing patterns. The main limitation lies in the signal-to-noise ratio (S/N). We also attempted to include all available data over the past six years. However, the light curves are sparsely and unevenly distributed (two consecutive sectors followed by a two-year gap), so the frequency resolution was hardly improved, while introducing a complex window function. Moreover, the S/N did not improve meaningfully because instrumental effects occur over the five-year baseline (see another similar discussion by Scott & Bowman 2026).

Figure 1 shows the period-spacing pattern of TIC 306384085. We demonstrate that two consecutive TESS sectors are sufficient to identify g-mode period-spacing patterns. This star exhibits a clear pattern in which the period spacing decreases linearly with increasing period. To explain the decreasing relation between period spacing and period in the regime of rapid rotation, where rotational effects cannot be treated perturbatively, we applied the traditional approximation of rotation (TAR). In this framework, the θ-component of the rotation vector is neglected, since g-mode wavenumbers are predominantly radial (Lee & Saio 1997; Townsend 2003; Bouabid et al. 2013; Van Reeth et al. 2016; Ouazzani et al. 2017; Saio et al. 2018a; Rui et al. 2024). By fitting the period spacing pattern assuming the TAR, we measured the near-core rotation rates $f_{\rm rot}$, and the asymptotic spacings Π_0 of the stars. The asymptotic spacing is defined as $\Pi_0 = 2\pi^2 \left(\int_{\rm gc} \frac{N}{r} \mathrm{d}r \right)^{-1}$, where N is the Brunt–Väisälä frequency, r is the local radius, and the integral is computed over the g-mode cavity (Aerts et al. 2010).

Figure 2 shows the posterior distributions of the near-core rotation rate and the asymptotic period spacing (Π_0) of TIC 306384085. We obtained $f_{\rm rot} = 2.70 \pm 0.03\,\mathrm{d}^{-1}$ and $\Pi_0 = 4660 \pm 80\,\mathrm{s}$. This star has a higher near-core rotation frequency than the median value of $\sim 1\,\mathrm{d}^{-1}$ found by Li et al. (2020b) for a sample of 611 galactic γ Dor stars monitored during 4 years by the *Kepler* space telescope. Furthermore, the Π_0 value of this star is also larger than the *Kepler* sample median of $\sim 4000\,\mathrm{s}$, suggesting that the star, and hence the cluster, is still near the beginning of the main-sequence phase. Figure 3 shows the best-fitting period-spacing pattern computed with the TAR, which reproduces the observed period spacings very well.

Table 1. Stellar parameters of the γ Dor stars with clear period spacing patterns in NGC 3532.

TIC	$(G_{\rm BP} - G_{\rm RP})_0$ (mag)	M ($\mathrm{M}_\odot$)	Π_0 (s)	$f_{\rm rot}$ (d^{-1})
305347034	0.42	1.491(24)	4580(240)	0.50(4)
306045270	0.42	1.496(24)	4710(150)	0.911(23)
305906846	0.40	1.511(23)	5060(210)	1.705(20)
306503414	0.39	1.518(23)	4220(160)	2.011(18)
305909136	0.30	1.604(27)	5400(400)	2.85(3)
306503983	0.28	1.623(28)	5900(500)	2.75(4)
306384085	0.27	1.625(27)	4670(170)	2.71(3)
306385060	0.17	1.76(4)	5250(210)	2.800(27)

Notes. Numbers in parentheses indicate the uncertainty in the last quoted digits.

We provide an exhaustive description of the frequency extraction, g-mode period-spacing identification, and the measurement of near-core rotation rates using the traditional approximation of rotation in Appendix A. Readers are further referred to the papers by Van Reeth et al. (2015b), Van Reeth et al. (2016), Li et al. (2019a), and Li et al. (2020b) for more details. We also show all the identified period spacing patterns of the other g-mode pulsators in NGC 3532 in Appendix A, from Fig. A.6 to A.12. We list the intrinsic Gaia colour indices, isochrone-derived masses, Π_0, and $f_{\rm rot}$ of these stars in Table 1. A more detailed discussion of the near-core rotation rates as a function of stellar mass is given in Sect. 5.2.

Figure 4 shows the CMD of NGC 3532 and the locations of the eight g-mode pulsators with clear period-spacing patterns identified in this work. We find that all these stars are located on the single-star main sequence, showing no evidence of high-mass-ratio binarity. TIC 306385060 is somewhat ambiguous, as it is unclear whether it lies within the extended main-sequence turnoff region or is a multiple system. We also notice that stars with higher near-core rotation rates ($\gtrsim 2\,\mathrm{d}^{-1}$) tend to lie near the red edge of the CMD, whereas slower rotators preferentially occupy the blue edge, implying a clear effect of gravity darkening. Beyond the stars with g-mode period-spacing patterns, we also measured rotation rates for stars showing modes but no clear pattern. For these, we used the dominant frequency to derive their near-core rotation rates, following the methods of Sepulveda et al. (2022), Sepulveda et al. (2023), and Aerts et al. (2025). A detailed discussion of these results is provided in Appendix B.

3.3. Contamination check

Because the field of view around NGC 3532 is highly crowded, we could not simply reject stars based on the fraction of contaminating light from neighbouring sources, as this would remove almost all potential candidates. Instead, we adopted an alternative approach to assess the contamination level. Specifically, we examined whether any nearby star lies within 63″ of the target and is brighter than the target magnitude plus four. This method identifies all possible contamination sources within three TESS pixels that contribute more than 2.5% of the target's flux. Furthermore, we examined the Gaia effective temperature or colour

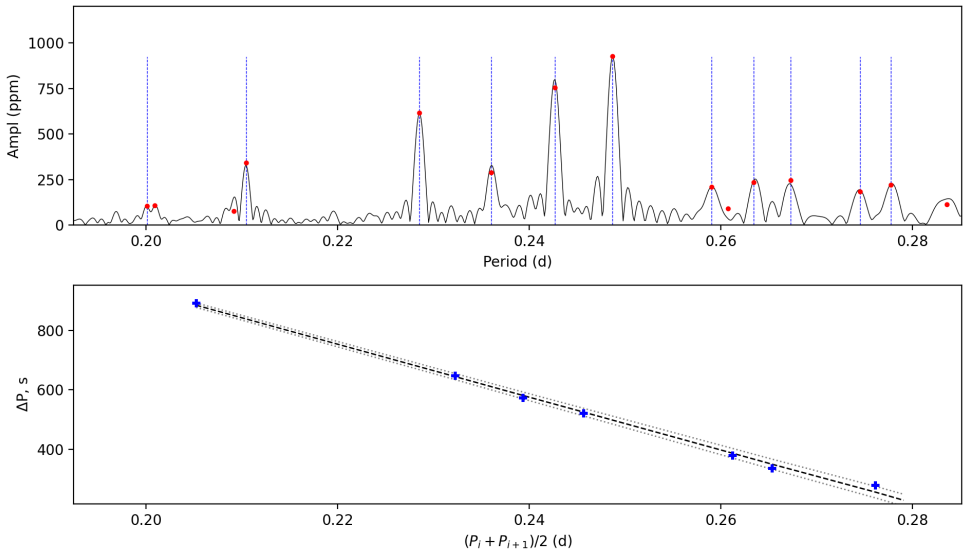

Fig. 1. Amplitude spectrum and period-spacing pattern of TIC 306384085 as a function of pulsation period, based on the two consecutive TESS sectors 63 and 64. *Top:* Amplitude spectrum versus period. The red dots mark the pulsation signals extracted by the prewhitening procedure, while the blue vertical dotted lines indicate the g-mode periods used to calculate the period spacings shown in the bottom panel. *Bottom:* Period spacings as a function of the mean period, $(P_i + P_{i+1})/2$. The blue crosses represent the measured period spacings, which require two consecutive periods to be identified. The dashed line shows the linear fit, and the dotted lines indicate its uncertainty region.

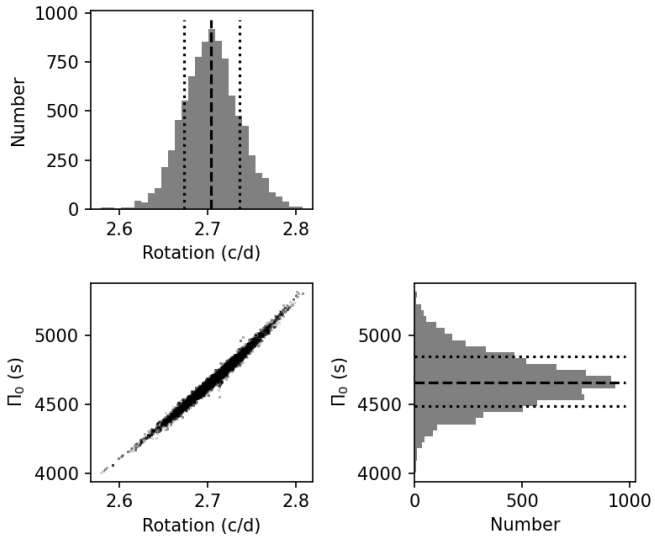

Fig. 2. Posterior distributions of the near-core rotation rate and the asymptotic spacing Π_0 of TIC 306384085.

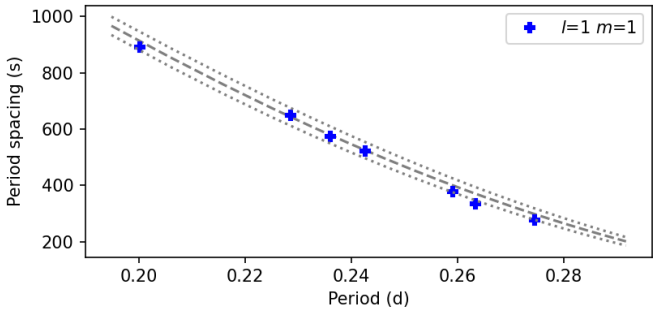

Fig. 3. Best-fitting period spacing pattern of TIC 306384085 based on the near-core rotation rate and the Π_0 value in Fig. 2.

index to assess whether each star lies within the region of g-mode main-sequence stars.

We found that TIC 305347034, 306503983, 306384085, and 306385060 have no nearby stars satisfying the above criteria, implying a clear flux source. The stars TIC 305906846, 306045270, and 306503414 do have some neighbour stars that satisfy the above criteria, but those with high temperatures are too faint (close to the magnitude cut) to provide significant pulsation signals. However, TIC 305909136 and TIC 305909160 are severely contaminated by each other. These two stars exhibit nearly identical period-spacing patterns, corresponding to the same $f_{\rm rot}$ and Π_0. A pixel-level frequency-spectrum analysis of the TESS full-frame images centred on TIC 305909160 shows that the pulsation amplitudes increase toward the lower-left pixel, closest to TIC 305909136. We therefore keep TIC 305909136 as the likely pulsating source and remove TIC 305909160 from the sample of g-mode pulsators. In addition, there is a third nearby source, TIC 306048083, but its effective temperature ($\sim$ 6207 K) is low and it can therefore be excluded.

4. PARSEC isochrone fittings of NGC 3532 and NGC 2516

Li et al. (2024a) provided isochrone fitting for NGC 2516 using MIST models (Choi et al. 2016; Dotter 2016), whereas isochrone fitting of NGC 3532 was carried out by He et al. (2025) based on PARSEC isochrone models (version 2.0S; Nguyen et al. 2022). In this work, we follow the methodological framework of He et al. (2025) to fit an isochrone of NGC 2516, and we compare our results with those of Li et al. (2024a), which are based on a MIST isochrone.

The membership of NGC 2516 was provided by Pang et al. (2021). Although a different member-star identification was used compared to the work by Li et al. (2024a), who used the catalogue by Meingast et al. (2021), the impact should be negligible, as the overall shape of the CMD is not affected by several non-overlapping stars. The adopted PARSEC isochrones used the RV = 3.1 extinction curves from Cardelli et al. (1989) and O'Donnell (1994) to compute the extinction coefficients for the Gaia bands. The metallicity of the isochrones was fixed at solar value, which is $Z_\odot$ = 0.0152 (Caffau et al. 2011; Bressan et al. 2012). For both clusters, we used non-rotating PARSEC isochrone models. Rotational effects — such as rotational mixing and gravity darkening — shift stars toward the red side of the CMD, but the underlying physics remains highly uncertain. Therefore, we prefer to rely on non-rotating PARSEC models,

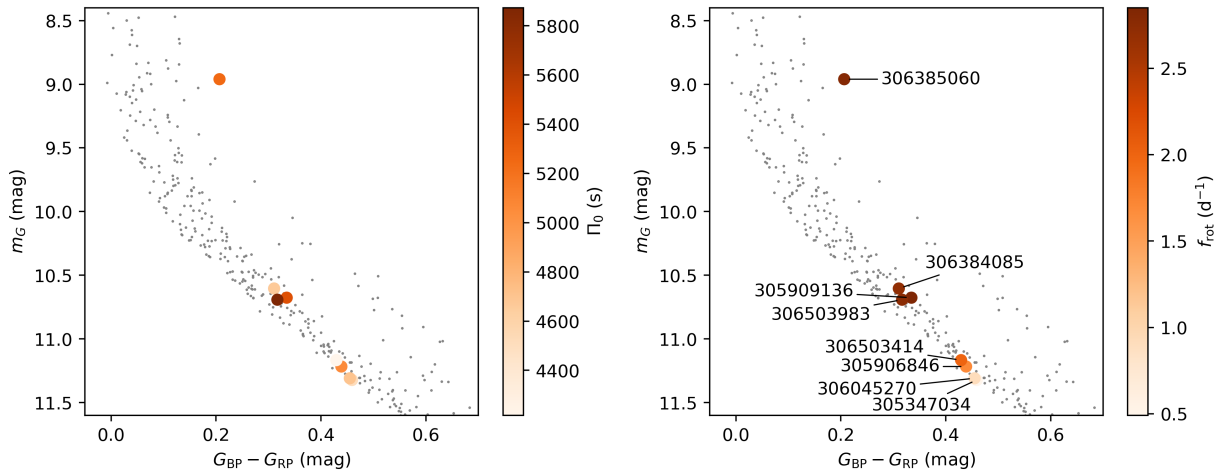

Fig. 4. CMD of NGC 3532 showing the eight identified g-mode pulsators listed in Table 1. The grey dots represent all the cluster members, and the extinction correction has not been applied. The left and right panels are colour-coded by the asymptotic period spacing Π_0 and the near-core rotation rate f_{rot}, respectively. We show the TIC numbers in the right panel.

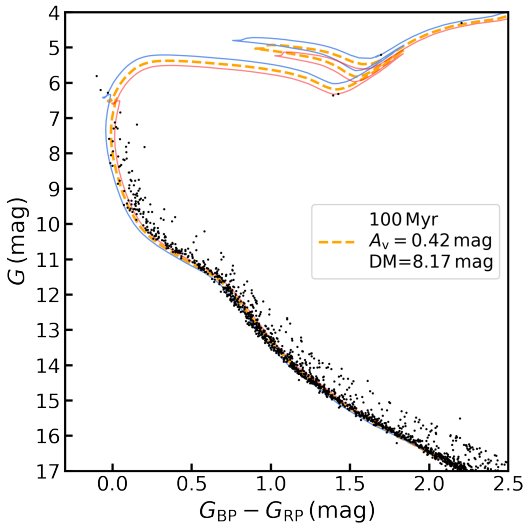

Fig. 5. PARSEC isochrone fitting of NGC 2516. The best-fitting isochrone, with an age of 100 Myr, extinction A_v = 0.42 mag, and distance modulus (DM) of 8.17 mag, is shown by the yellow thick dashed line. The blue and red lines indicate the uncertainty range of the isochrone, accounting for the shifts in age, extinction, and distance modulus.

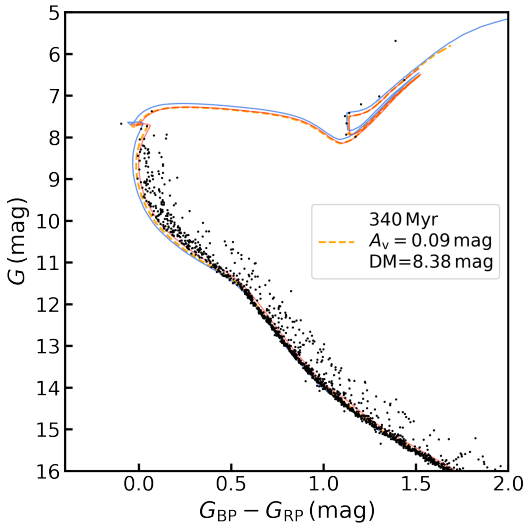

Fig. 6. Same as Fig. 5 but for NGC 3532.

Table 2. Isochrone fitting results of NGC 2516 and NGC 3532.

Cluster	Age (Myr)	A_v (mag)	$m - M$ (mag)
NGC 2516	100^{+10}_{-10}	$0.42^{+0.03}_{-0.05}$	$8.17^{+0.05}_{-0.05}$
NGC 3532	340^{+10}_{-20}	$0.09^{+0.02}_{-0.02}$	$8.38^{+0.03}_{-0.07}$

while only requiring the isochrone to align with the blue edge of the hot part of observed CMD ($T_{eff} \gtrsim 6500$ K, where the slope of the main sequence changes slightly). This criterion is difficult to define mathematically, so we rely on visual fitting. This yielded the best-fitting extinction A_v = 0.42 mag, the age of NGC 2516 $t_{NGC\,2516}$ = 100 Myr, and the distance modulus $m - M$ = 8.17 mag. We also estimated the uncertainties by fixing the age and the distance modulus at their best-fitting values and varied the extinction A_v to visually determine the value at which an obvious deviation from the observed CMD appears. The same procedure was applied to the age and the distance modulus. Figure 5 displays the best-fitting PARSEC isochrone and the uncertainty ranges. We also applied the same steps to NGC 3532 and derived its fitting uncertainties, as shown in Fig. 6 because these were not reported by He et al. (2025). The best-fitting results for both clusters are listed in Table 2. For the age of NGC 2516, we derived a value very similar to that obtained from the MIST rotating isochrone models by Li et al. (2024a) (100 ± 10 Myr versus 102 ± 15 Myr). In contrast, several other previous studies based on different age-dating methods—such as gyrochronology, lithium depletion, and g-mode asteroseismology—reported slightly older ages, ranging from 130 to 150 Myr (Meynet et al. 1993; Sung et al. 2002; Bouma et al. 2021; Fritzewski et al. 2020; Li et al. 2025). The extinction of NGC 2516 is consistent with previous studies (Sung et al. 2002; Li et al. 2025).

We calculated the masses of the main-sequence pulsating stars in both clusters by interpolating the relation between the G-band magnitude and PARSEC-derived mass. For NGC 2516, Li et al. (2025) measured the masses of six pulsating stars

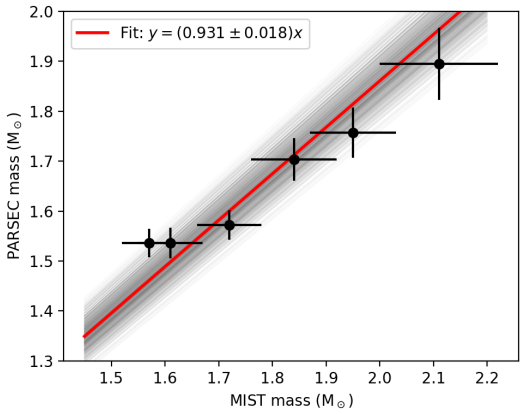

Fig. 7. Masses of six g-mode pulsators in NGC 2516, derived from the PARSEC and MIST isochrone fittings. The red line shows the best-fitting direct proportionality relation, $y = (0.931 \pm 0.018)x$, which means that the PARSEC masses are 93.1% ± 1.8% of the MIST masses. The gray area shows the uncertainty of the linear fitting.

in NGC 2516 using the best-fitting MIST isochrone. Here we compare them in Fig. 7. Overall the two mass estimates agree well keeping in mind the uncertainties. By fitting a linear function through the origin, we find that the masses derived by the PARSEC isochrone are equal to 93.1% ± 1.8% of the MIST isochronal values, that is, somewhat smaller. These mass differences may partly arise from differences in the adopted input physics between the PARSEC and MIST models, for example, the assumed solar metallicity ($Z_\odot$ = 0.0152 versus 0.014; Asplund et al. 2009; Paxton et al. 2011). These newly derived masses from the PARSEC isochrone fitting help resolve the small mass discrepancy between the seismic masses and the MIST-derived masses in NGC 2516. As shown by Li et al. (2025), the two most massive g-mode pulsators in NGC 2516, TIC 372912679 and TIC 308992761, have MIST-derived masses of $1.95 \pm 0.08\,M_\odot$ and $2.11 \pm 0.11\,M_\odot$, respectively. Their seismic masses—obtained by comparing their g-mode asymptotic spacings with the MESA-based asteroseismic grid of Mombarg et al. (2024b)—are only about $1.70\,M_\odot$ and $1.76\,M_\odot$. Our new PARSEC masses for these two stars, 1.75 ± 0.05 and $1.89 \pm 0.07\,M_\odot$, are consistent with the seismic masses within 1σ and 2σ for TIC 372912679 and TIC 308992761, respectively.

5. Asteroseismic results

5.1. Observed γ Dor instability strip

Figure 8 shows the CMDs of both NGC 3532 and NGC 2516. We corrected the extinction effects on the *Gaia* colour index derived from our isochrone fitting results. The correction appears to work well, as the lower parts of the main sequences of the two clusters are well aligned, while the stars with higher masses in NGC 3532 have evolved to the right. In addition, since NGC 3532 is about 240 Myr older than NGC 2516, the upper part of its main sequence has evolved toward the red, and its main-sequence turn-off appears lower than that of NGC 2516.

During the process of period spacing identification, we noticed that many γ Dor stars do not exhibit clear period-spacing patterns; instead, they display a broad hump in the low-frequency region. Such a hump can be distinguished from that caused by surface modulation, which typically produces a relatively narrower peak caused by the rotation frequency. We also

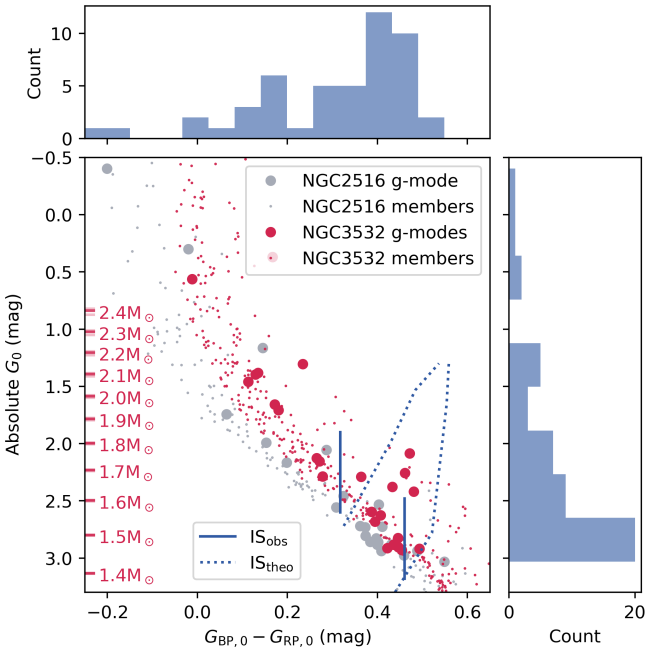

Fig. 8. Extinction-corrected CMD of NGC 3532 (red) and NGC 2516 (grey). The main panel shows the observed CMD, with the x-axis representing the intrinsic *Gaia* colour $G_{BP,0} - G_{RP,0}$ and the y-axis showing the absolute *Gaia* G-band magnitude. Mass ticks from the best-fitting isochrone of NGC 3532 are also shown in red. Theoretical and observational instability strips of γ Dor stars taken from the literature are plotted in blue dashed or solid lines. The histogram on the top displays the distribution of g-mode pulsators as a function of colour index, while the histogram on the right shows their distribution in absolute G-band magnitude.

distinguished these unresolved g modes from Rossby modes, which typically exhibit a hump-and-spike feature or a distinctive amplitude profile (Saio et al. 2018b; Henriksen et al. 2023; Antoci et al. 2025). Nevertheless, some stars may be misclassified because the light curves are relatively short. We therefore show all the g-mode pulsators in NGC 3532 and NGC 2516 on the CMD in Fig. 8, regardless of whether they exhibit clear g-mode period-spacing patterns.

A dense region occurs in the lower-right corner of the CMD where most g-mode pulsators are located. We then overlay the instability strip (IS) by Dupret et al. (2005) and find that the theoretical IS of γ Dor stars roughly corresponds to this dense region, with an agreeing red edge around ~ 7000 K. We therefore infer that the dense region in the lower-right corner of the CMDs corresponds to the γ Dor IS in which g modes are excited by the flux-blocking mechanism. We visualise the observational instability range by means of two histograms as a function of the intrinsic *Gaia* colour (top) and absolute magnitude (right) in Fig. 8. In the top panel of Fig. 8, we find that the colour distribution of the g-mode pulsators is bimodal: most stars are located at $G_{BP,0} - G_{RP,0} > 0.26$ mag, corresponding to the γ Dor stars mentioned above, while another group of stars shows bluer *Gaia* colours (i.e., higher temperatures).

To quantify the width of the red component of the bimodal colour distribution, we selected the stars with $G_{BP,0} - G_{RP,0} > 0.26$ mag, excluded the four stars lying above the main sequence (likely due to binarity), and fitted a Gaussian function to their colour distribution. We assumed that the colour index $G_{BP,0} - G_{RP,0}$ follows a Gaussian distribution, $G_{BP,0} - G_{RP,0} \sim$

$\mathcal{N}\left(\mu, \sigma_i^2 + \sigma_{\rm int}^2\right)$, where μ is its mean value and $\sigma_{\rm int}$ its intrinsic width. The observational uncertainty of the colour index, σ_i, was set to 0.056 mag, which corresponds to the intrinsic scatter of the main sequence of NGC 2516 reported by Li et al. (2024a). This observational uncertainty accounts for various physical effects that can broaden the observed main sequence, such as differential extinction, unresolved binaries, slight distance spread, and rotational effects, including both evolutionary influences and gravity darkening due to different inclinations. The likelihood is defined as

$$\ln L = -\frac{1}{2}\sum_i \left[\ln\left(\sigma_i^2 + \sigma_{\rm int}^2\right) + \frac{\left(G_{\rm BP,0,i} - G_{\rm RP,0,i} - \mu\right)^2}{\sigma_i^2 + \sigma_{\rm int}^2}\right]. \quad (1)$$

We then ran a Markov-chain Monte Carlo algorithm to obtain the best-fitting values and the uncertainties of μ and $\sigma_{\rm int}$.

The best-fitting mean value of the colour index is 0.389 ± 0.013 mag, with an intrinsic Gaussian width of 0.045 ± 0.017 mag. We define the boundaries of the observational IS as the $\pm 2\sigma$ range. In this way, we find that the IS red edge is consistent with previous theoretical predictions:

$$\text{red edge:} \quad G_{\rm BP,0} - G_{\rm RP,0} = 0.48 \pm 0.04\,\text{mag}, \quad (2)$$

$$\text{blue edge:} \quad G_{\rm BP,0} - G_{\rm RP,0} = 0.30 \pm 0.04\,\text{mag}. \quad (3)$$

We further convert these colour boundaries to effective temperatures based on the best-fitting PARSEC isochrone of NGC 3532:

$$\text{red edge:} \quad T_{\rm eff} = 7070 \pm 120\,\text{K}, \quad (4)$$

$$\text{blue edge:} \quad T_{\rm eff} = 7760 \pm 160\,\text{K}. \quad (5)$$

The luminosities of the red and blue edges on the best-fitting PARSEC isochrone of NGC 3532 are $\log(L_{\rm red}/L_\odot) = 0.65 \pm 0.04$ and $\log(L_{\rm blue}/L_\odot) = 0.87 \pm 0.04$.

By comparing the observational IS with the theoretical one from Dupret et al. (2005) based on the flux blocking mechanism, we find that our observed IS defined by the $\pm 2\sigma$ region aligns well with the bottom of the theoretical one, as shown in Fig. 8. Another theoretical prediction of the IS of γ Dor stars was provided by Bouabid et al. (2013), taking into account the effects of fast rotation on the flux blocking excitation mechanism. That work predicted a temperature range from ~ 7400 K to ~ 6600 K and showed that the pulsation period in the co-rotating frame increases with decreasing temperature. Çakırlı et al. (2025) reported an observational instability strip with a similar temperature range to that predicted by Bouabid et al. (2013), based on a sample of eclipsing binaries with g-mode pulsators. Our observed IS appears at higher temperatures, which may be because the stars in our sample are still very young and rotate rapidly. Li et al. (2020b) reported the temperature distribution of 611 γ Dor stars in the *Kepler* field and found an over-density region at ~ 7300 K, which coincides with the observed IS in this work.

In addition, we find a considerable number of hot g-mode pulsators with masses larger than those predicted by the classical γ Dor IS based on the flux blocking mechanism alone. These hot g-mode pulsators have also been identified among Galactic field stars (Gaia Collaboration et al. 2023; Aerts et al. 2023; Hey & Aerts 2024) and in other clusters (Mowlavi et al. 2013). They populate the region between the classical γ Dor IS and the SPB IS, although with a lower density of pulsators (Mombarg et al. 2024b). Various explanations can be suggested for this. From an observational perspective, several factors can shift the observed positions of stars in the CMD, such as fast rotation, differential extinction, or metallicity. However, these effects are unlikely to cause shifts of several solar masses. From a theoretical perspective, the broad mass distribution from $\sim 1.6\,M_\odot$ to $\sim 3\,M_\odot$ needs more modelling work in terms of mode excitation computations. While flux blocking is a very efficient mechanism for cool γ Dor stars, the hotter ones occur in the δ Sct IS caused by the opacity mechanism (the so-called κ mechanism, Pamyatnykh 1999; Grigahcène et al. 2010; Antoci et al. 2014; Grassitelli et al. 2015; Xiong et al. 2016). On the even hotter end, it has been shown that rotation at half of the critical rate pushes the cool border of the SPB IS downwards towards masses well below $3\,M_\odot$ for prograde sectoral modes (Szewczuk & Daszyńska-Daszkiewicz 2017). Finally, most instability computations do not include radiative levitation. However, Rehm et al. (2024) showed that, in SPB-star models rotating at 20% of the critical rate, radiative levitation excites more modes at earlier evolutionary stages and shifts the blue edge of the instability strip to higher temperatures. Similar studies of the interplay between radiative levitation and fast rotation have not yet been carried out for stars with masses between 2 and $3\,M_\odot$. Nevertheless, such effects are also likely to influence mode excitation in this mass range, potentially explaining some of the hottest g-mode pulsators found in NGC 3532, as well as in similar clusters and in the Galactic field.

5.2. Near-core rotation rates

Figure 9 displays the near-core rotation rates of the member stars in both NGC 3532 and NGC 2516 as a function of stellar mass. We derived the stellar masses by interpolating the relation between mass and the Gaia G-band magnitude from the best-fitting PARSEC isochrones. The mass uncertainties were estimated from two sources. First, the model-related uncertainty arises from the visual fitting steps. Second, the observational uncertainty accounts for the intrinsic spread of the main sequence, reflecting effects such as gravity darkening and differential extinction, as well as other unresolved factors. In the upper part of Fig. 9, we also plot the Keplerian critical rotation rates derived from the best-fitting isochrones for NGC 3532 and NGC 2516. Multiple curves are shown to estimate the model uncertainties arising from the visual fitting steps. We find that in NGC 3532, as the stars expand during their evolution, their critical rotation rates decrease, and this effect is more apparent in the high-mass range. The stars in both NGC 3532 and NGC 2516 are rotating at approximately 50% of their critical rotation rates.

We find that both clusters show similar rotation–mass relations. The stars exhibit two distinct behaviours below and above $\sim 1.6\,M_\odot$. For the lower-mass stars ($M \lesssim 1.6\,M_\odot$), the rotation rates increase with mass in both clusters. When the stellar mass exceeds $\sim 1.6\,M_\odot$, the stars rotate more rapidly and display comparable rotation rates, forming rotation plateaus. For NGC 3532, these high-mass stars form a rotation plateau around $\sim 2.8\,\text{d}^{-1}$, which is slightly below the one of NGC 2516 ($\sim 3.0\,\text{d}^{-1}$). We further quantitatively measure the rotation plateaus of NGC 3532 and NGC 2516. Similar to the steps in Section 5.1, we again assume that the stellar rotation rates in each cluster obey a Gaussian distribution $f_{{\rm rot},i} \sim \mathcal{N}\left(\mu, \sigma_i^2 + \sigma_{\rm int}^2\right)$, where μ now is the mean value of the rotation plateau, $\sigma_{\rm int}$ its intrinsic width, and σ_i is the observed uncertainty of $f_{\rm rot}$. We define the same likelihood as Eq. 1. By maximising the likelihood, we obtain: $\mu_{\rm NGC2516} = 2.966^{+0.010}_{-0.009}\,\text{d}^{-1}$, $\sigma_{\rm int,NGC2516} = 0.021^{+0.013}_{-0.008}\,\text{d}^{-1}$, and $\mu_{\rm NGC3532} = 2.78^{+0.05}_{-0.05}\,\text{d}^{-1}$, $\sigma_{\rm int,NGC3532} = 0.08^{+0.09}_{-0.04}\,\text{d}^{-1}$. The probability that $\mu_{\rm NGC2516}$ is larger than $\mu_{\rm NGC3532}$ is 0.9867, indicating a statistically significant spin-down trend. The rate of the spin-down is roughly $-0.0009^{+0.0003}_{-0.0005}\,\text{d}^{-1}\,\text{Myr}^{-1}$. We connect this to

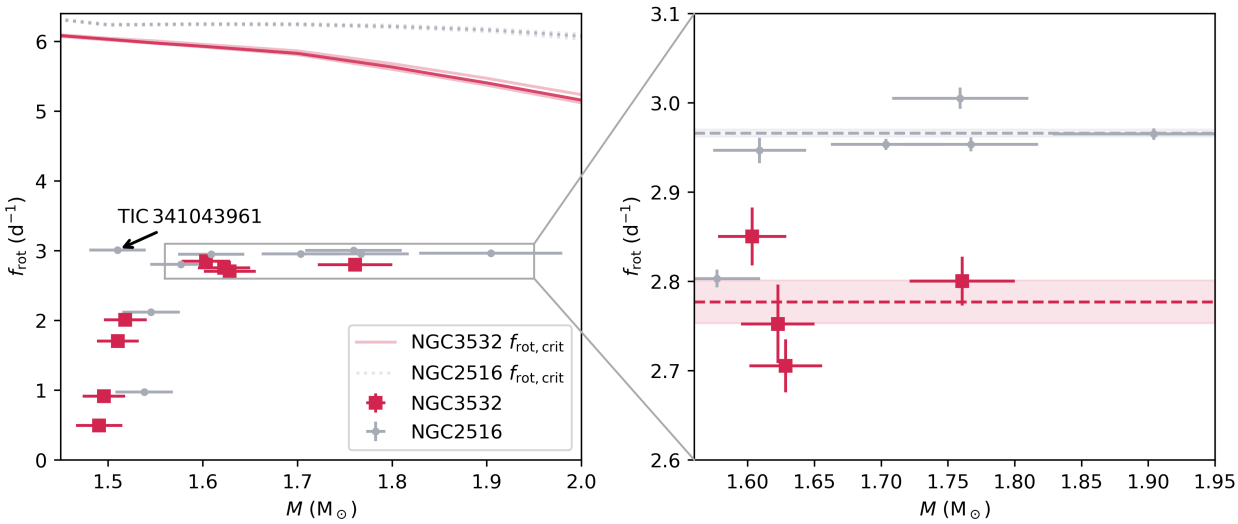

Fig. 9. Left panel: near-core rotation rates as a function of stellar mass for the g-mode pulsators with clear period spacing patterns in NGC 3532 (red) and NGC 2516 (grey). The critical rotation rates are plotted at the top, with solid red lines representing NGC 3532 and dotted grey lines representing NGC 2516. Multiple critical rotation rate curves are shown for each cluster to illustrate the effects of isochrone-fitting uncertainties. TIC 341043961 shows a high rotation rate at the lower-mass end due to binarity. Right panel: a zoom-in on the higher-mass stars, whose masses range from $\sim$ 1.6 M$_\odot$ to $\sim$ 1.9 M$_\odot$. The horizontal dashed lines mark the rotation plateaus of each cluster, and the shaded areas indicate their uncertainties.

the age uncertainties of the two clusters in Section 5.3. The intrinsic width of the rotation plateaus of both clusters points to an increase by a factor of 3.8, implying an accumulated effect of different internal physical processes on AM transport.

We next discuss the spin-down mechanisms of stars with masses below and above 1.6 M$_\odot$, respectively.

For the stars below 1.6 M$_\odot$, we infer from our cluster observations that a braking mechanism due to AM loss should be responsible for the more efficient slowdown of those cluster members with a mass below $\sim$ 1.6 M$_\odot$. We hypothesize that these stars are spun down by magnetised stellar winds that cause modest mass loss rates. Stars with masses below a certain threshold (the so-called Kraft break occurring near $T_{\rm eff} \approx 6500$ K; Kraft 1967; Wang et al. 2026b) have thick convective envelopes, which drive magnetic dynamos and hence yield magnetised stellar winds (e.g. Noyes et al. 1984; Wright et al. 2011; Gallet & Bouvier 2013). These winds carry AM and slow the stellar rotation (Weber & Davis 1967; Kraft 1967; Réville et al. 2015). Beyer & White (2024) deduced a mass threshold of about 1.4 M$_\odot$ for the Kraft break, based on a large sample of middle-aged galactic stars. Given the strong (M, Z) relation, uncertainties in metallicity measurements, and the lack of very young stars in the sample used by Beyer & White (2024), a $\sim$ 25% transition range in the mass estimate for the Kraft break makes sense. As stellar mass increases from solar-like dwarfs to the range of the g-mode pulsators found in NGC 3532 and NGC 2516, the convective envelopes become thinner. This weakens magnetic braking while allowing g modes to be excited by the flux-blocking mechanism and to propagate to the surface (e.g. Guzik et al. 2000; Dupret et al. 2005). This explains the observed mass-dependence of the spin-down we observe in the two clusters. In Fig. B.2 of Appendix B, we confirm this rotation–mass relation by using the dominant g modes in stars.

For the stars above $\sim$ 1.6 M$_\odot$, we find that both clusters show rotation plateaus ($\sim$ 2.8 d^{-1} for NGC 3532 and $\sim$ 3.0 d^{-1} for NGC 2516). The slightly slower near-core rotation rates observed in NGC 3532 reflect the expected spin-down of the internal region adjacent to the convective core due to AM transport as intermediate-mass stars evolve along the main sequence, as predicted by previous asteroseismic studies (e.g. Ouazzani et al. 2019; Pedersen 2022; Moyano et al. 2023; Mombarg 2023). In this region, the surface convective layers become too thin to have any strong impact on rotation and the AM loss totally disappears at the high-mass end, as also observed in galactic stars (Aerts 2025). For these more massive stars, the slowdown near the core is solely a result of internal AM transport and redistribution inside the star. These recent asteroseismic results are in agreement with older photometric studies of clusters based on extended features of their CMD distributions (e.g., Mackey et al. 2008; Milone et al. 2009, 2018; Cordoni et al. 2018). This feature was found to be caused by their different rotation rates (e.g., Bastian & de Mink 2009; Milone et al. 2018; Cordoni et al. 2018), with widely distributed measured $v \sin i$ from 0 to 400 km s^{-1} (e.g., Marino et al. 2018a; Sun et al. 2019b; Kamann et al. 2020). The asteroseismic distributions of the broad ranges in equatorial rotation velocities and specific AM of galactic stars found by Aerts (2025) are in agreement with the cluster results, keeping in mind that the cluster stars are younger. All these studies together reveal the existence of large populations of rapidly rotating stars with large masses, indicating that magnetic braking via AM loss is absent in most of these hot stars. Instead, star-disc interactions at the pre-MS stage (Bastian et al. 2020), binary mergers (Wang et al. 2022) or tidal effects (D'Antona et al. 2015, 2017; Li et al. 2020a) can account for the formation of slow rotators in these samples of intermediate-mass stars with radiative envelopes.

5.3. Predicted rotation rates by existing model

We examined whether the asteroseismically calibrated models computed by Mombarg et al. (2024a) can reproduce the observed near-core rotation rates of the stars heavier than 1.6 M$_\odot$ in NGC 3532 and NGC 2516, where the AM loss can be neglected. We point out that these models were constructed to explain the seismic properties of a large sample of galactic stars, while

younger stars as in our clusters were under-represented. They were computed for the solar mixture and metallicity $Z = 0.014$, following Asplund et al. (2009). In Fig. 10, we compare the model-predicted rotation rates as a function of time with the observed values. Instead of adopting the ages derived from our PARSEC isochrone fitting listed in Table 2, we assigned broader age ranges estimated from previous studies based on various age-dating methods, as discussed above. For NGC 2516, we adopted an age range of 125 ± 30 Myr, while for NGC 3532, we used 340 ± 60 Myr. We selected stellar evolution models with stellar masses of 1.7 and 1.9 $M_\odot$, covering the mass range of the fast rotators, with two values of the convective core overshooting, $f_{\rm CBM} = 0.005$ and 0.025. Because the observed rotation rates are relatively high, we adopted the most rapidly rotating models, with initial rotation rates equal to 55% of the critical rotation rate.

We find that the predicted spin-down rate depends on both stellar mass and the adopted overshooting parameter. Higher-mass models spin down more rapidly than lower-mass ones, because they evolve faster. In addition, models with lower core overshooting experience a stronger spin-down. Despite these trends, none of the models can reproduce the observed near-core rotation rates for the high-mass g-mode pulsators in either cluster. For NGC 3532, the lower-mass models only intersect the lower boundary of the observed rotation range, whereas the higher-mass models predict rotation rates that are systematically too low. The discrepancy is even more severe for NGC 2516: its stars rotate faster than predicted even by the most rapidly rotating models, which start at 55% of the critical rotation rate and assume uniform rotation at the zero-age main sequence (ZAMS). While several studies have shown that isolated galactic γ Dor stars are generally close to uniform rotators (Van Reeth et al. 2018; Li et al. 2020b; Saio et al. 2021), this assumption may not hold for very young cluster stars. We also note that the implementation of AM transport used by Mombarg et al. (2024a) can lead models with high initial rotation to reach the critical rotation rate during the main sequence.

Our findings suggest that the initial rotation rates required to explain the observed values in NGC 3532 and NGC 2516 must be higher than 55% of the critical rate. Moreover, Fig. 10 suggests that the initial rotation rate varies with stellar mass in order for evolutionary tracks of different masses to pass through the observed near-core rotation frequencies of both clusters. We further investigate this in the next section.

5.4. Near-core rotation rates assuming AM conservation

The AM-transport prescriptions adopted by Mombarg (2023) and Mombarg et al. (2024a) were calibrated to explain the asteroseismic measurements of a large sample of middle-aged galactic pulsators. The initial AM content of the young stars in our two clusters remains uncertain, because star formation models do not yet provide firm predictions for the earliest evolutionary phases. Therefore, we also tested simplified toy models with the aim of learning more about AM-transport physics at the youngest ages.

We still assume that AM is conserved throughout the early evolution and that differential rotation is negligible. The initial AM, $J_{\rm init}$, at the ZAMS is calculated using the formula,

$$J_{\rm init} = \Omega_{\rm init}\, I_{\rm init} = \frac{2}{3}\,\Omega_{\rm init} \int_0^M r^2\, {\rm d}m, \tag{6}$$

where r is the radial coordinate, $I_{\rm init}$ is the initial moment of inertia calculated by summing the spherical shells of mass dm multiplied by r^2 at radius r, R is the stellar radius, and $\Omega_{\rm init}$ is the initial rotation angular frequency. At time t, the angular rotation frequency $\Omega \equiv 2\pi f$ then follows as

$$f_t = f_{\rm init} \frac{I_{\rm init}}{I_t}, \tag{7}$$

where I_t is the moment of inertia at time t, computed from stellar models.

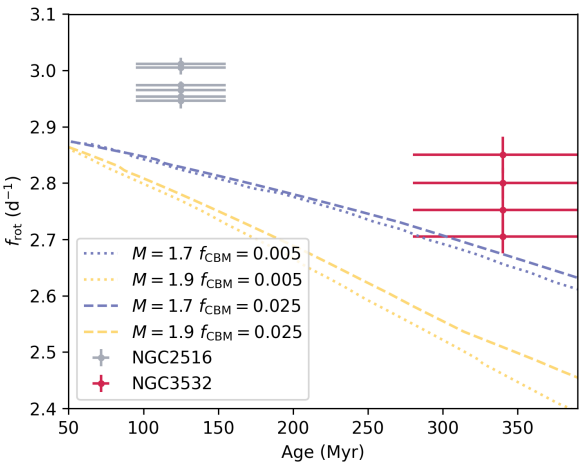

Fig. 10. Model-predicted near-core rotation rates as a function of age. The observations are the stars with mass larger than 1.7 $M_\odot$ from NGC 3532 and NGC 2516. The models were calculated by Mombarg et al. (2024a) with initial rotation rates of 55% of the critical rotation rates. We selected four models with masses of 1.8 and 2.1 $M_\odot$, covering the observed mass range, and with $f_{\rm CBM} = 0.005$ and 0.025.

To calculate the time-dependent moment of inertia I_t, we used the stellar profiles computed by Li et al. (2025) for the asteroseismic modelling of the g-mode pulsators in NGC 2516. Rotational mixing was included assuming an initial rotation rate of 50% of the critical rotation rate, in order to account for the effects of rapid rotation on stellar evolution. We chose two representative stellar masses, 1.70 and 1.90 $M_\odot$, to cover the mass range inferred from the isochrones, and we tested two overshooting values, $f_{\rm CBM} = 0.005$ and 0.025. We then adjusted the initial rotation rates, $f_{\rm init}$, for our stellar models to reproduce the observed near-core rotation rates in NGC 3532 and NGC 2516. We required that the models with different masses yield approximately the same rotation rates at the respective cluster ages, as no clear mass-dependent rotation trend is observed.

For NGC 2516, we find that initial rotation rates of 3.02 d^{-1} for the models with $M = 1.70\,M_\odot$ and 3.08 d^{-1} for $M = 1.90\,M_\odot$ successfully reproduce the observed rotation rates, as shown in Fig.11. The model-predicted rotation rates also show a natural spread that is comparable to the observed spread resulting from the different adopted overshooting values. As the models evolve up to $\sim$ 300 Myr, the predicted rotation rates also intersect the observed values of NGC 3532. However, our toy models predict a mass-dependent rotation rates for the stars in NGC 3532, namely the lower-mass stars should present higher rotation rates, which are not supported by our observations.

For NGC 3532, we find that an initial rotation rate of 2.93 d^{-1} for the 1.70 $M_\odot$ models and 3.16 d^{-1} for the 1.90 $M_\odot$ models intersect with the observed values at the cluster age. However, in this case, when the models are evolved backwards to the age of NGC 2516, the lower-mass stellar models exhibit rotation rates that are too slow, while the higher-mass models show rotation rates that are too fast (cf. Fig.11). Neither can reproduce the observed rotation rates of stars in NGC 2516. This suggests that

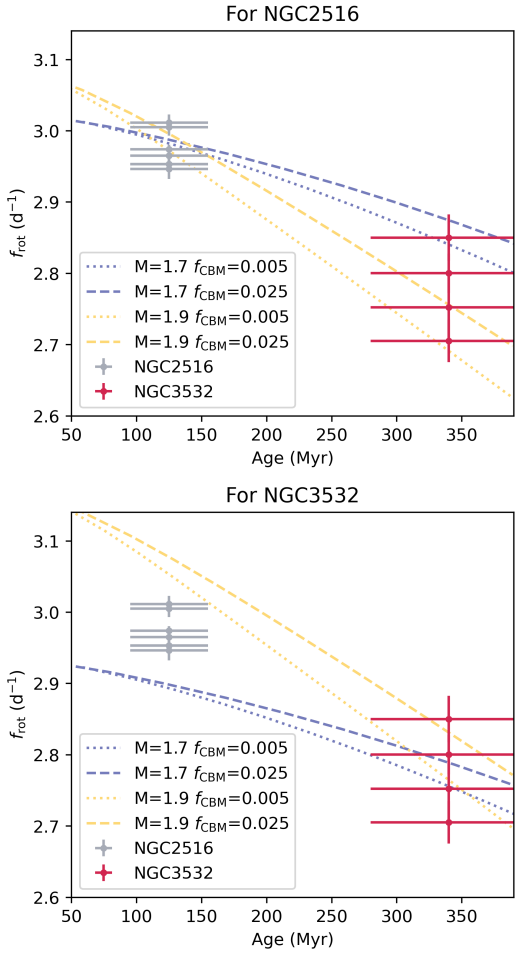

Fig. 11. Near-core rotation rate as a function of age, calculated under the assumption that AM is conserved throughout the stellar evolution. The evolutionary models were computed by Li et al. (2025) using the rotating one-dimensional `MESA` code. We selected two stellar masses, 1.7 and 1.9 $M_\odot$, to cover the mass range derived from isochrone fitting, combined with two convective core overshooting parameters, $f_{\rm CBM}$ = 0.005 and 0.025. The top and bottom panels show models with different initial rotation rates, chosen to reproduce the observed near-core rotation rates of the higher-mass g-mode pulsators in NGC 2516 and NGC 3532, respectively. In this figure, we only show the high-mass stars whose magnetic braking effects are negligible.

the two clusters had different initial rotation distributions if we insist that the AM loss is absent. We also find that the observed rotation distribution in NGC 3532 shows a larger spread, which cannot be explained by models with different overshooting values alone. This implies that additional AM birth and/or transport mechanisms may influence the rotational evolution, or that the cluster has a broader initial rotation distribution.

5.5. Tension between Π_0 and mass

The asteroseismic modelling work by Li et al. (2025) revealed a tension between the observed and theoretical Π_0 values of the two most massive g-mode pulsators in NGC 2516. Here, we extend this comparison to NGC 3532, where the discrepancy also occurs at lower mass. Figure 12 displays Π_0 as a function of stellar mass at the clusters' ages, which we refer to as the 'Π_0 isochrone'. The Π_0 values are extracted from the evolutionary models computed by Mombarg et al. (2024a), as used in Fig. 10.

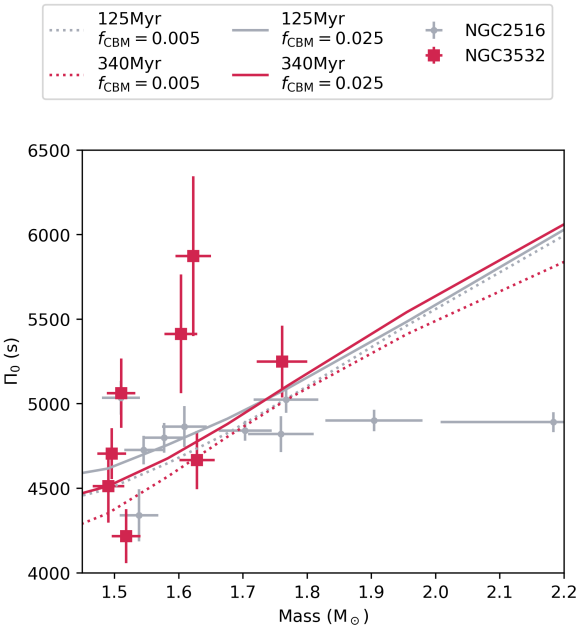

Fig. 12. Asymptotic spacing Π_0 as a function of stellar mass for the γ Dor stars in NGC 3532 (red) and NGC 2516 (grey). The theoretical values of Π_0 at given ages (the Π_0 isochrones) are taken from the model grid of Mombarg et al. (2024a). Four sets of Π_0 isochrones are shown: one for age of 125 Myr and another for 340 Myr, each computed with two different convective boundary mixing values, $f_{\rm CBM}$ = 0.005 and $f_{\rm CBM}$ = 0.025.

As the theoretical masses in the Π_0 isochrone are derived from MESA, while the observed stellar masses are obtained from PARSEC, we rescale the theoretical masses by a factor of 0.931 to ensure consistency. This factor is derived from Fig. 7. The theoretical Π_0 isochrones show a monotonic increase with stellar mass and only a slow decrease with age. Specifically, Π_0 increases from $\sim$ 4500 s at M = 1.5 $M_\odot$ to $\sim$ 5400 s at M = 1.9 $M_\odot$. Evolution has only a minor effect on Π_0 within the ages covered by the two clusters: at the low-mass end, Π_0 decreases by only a few hundred seconds from 125 Myr to 340 Myr, while remaining almost unchanged at 1.8 $M_\odot$. In addition, models with smaller $f_{\rm CBM}$ tend to yield smaller Π_0 values.

The observed Π_0 isochrones present a different picture. For NGC 2516, we do not see a clear correlation between Π_0 and stellar mass. Most stars exhibit Π_0 values distributed between $\sim$ 4700 s and $\sim$ 5000 s. At the high-mass end, the theoretical Π_0 values are much larger than the observed ones, making detailed asteroseismic modelling based on the grid in Mombarg et al. (2024a) inaccurate for these stars.

For NGC 3532, we do not observe a monotonic relation between Π_0 and mass. Rather, the stars display a range in Π_0. Some stars follow the theoretical Π_0 isochrones. However, other stars show large Π_0 values, reaching up to 5500–6000 s, which exceed the model predictions, although the measurement errors are large.

Currently, we do not have a satisfactory explanation for the tension between Π_0 and stellar mass, either from the theoretical or observational side. From an observational perspective, the first and most natural consideration is binarity. However, no double-lined absorption features were detected in the high-resolution FEROS spectra of the g-mode pulsators in NGC 2516 obtained with the ESO/MPG 2.2-m telescope at La Silla (Li et al. 2024a).

Removing stars that lie above the single-star main sequence also does not alleviate the tension. A second possibility is mass transfer or stellar merger processes, which may lead to inconsistencies between surface and core properties. Such processes can occur at early stages of cluster evolution (Wang et al. 2022). Alternatively, the tension between Π_0 and mass may be related to the well-known mass discrepancy. A similar Π_0 discrepancy has been reported in the g-mode pulsating binary KIC 10080943, whose asteroseismic masses are about 2σ lower than the dynamical masses (Keen et al. 2015; Schmid et al. 2015; Schmid & Aerts 2016). Discrepancies between dynamical, isochrone-based, and photometric masses have also been recognised before (e.g. Tkachenko et al. 2020; Sandquist et al. 2020).

5.6. Assessing possible binarity

In Fig. 9, we notice that TIC 341043961 in NGC 2516 shows an extremely fast rotation rate in the low-mass region. By checking the CMD in Li et al. (2024a), we find that TIC 341043961 lies above the single-star isochrone, so its fast rotation may be related to binarity. Tidal forces indeed significantly reshape the rotation of stars in binaries. For stars with radiative envelopes, the dynamical tide with radiative damping dominates the synchronisation process (Zahn 1975). The synchronisation time scale is $\tau_{\rm synch,rad} \sim (a/R)^{8.5}$, where a is the orbital semi-major axis and R is the stellar radius (Hurley et al. 2002). Both theory and observations confirm that strong tidal synchronisation tends to occur in short-period binaries for both late-type and early-type stars (i.e., $P_{\rm orb} \lesssim 10$ d, e.g., Lurie et al. 2017; Li et al. 2020a; Wang et al. 2026a).

The spectroscopic observations of the g-mode pulsators in NGC 2516 reported by Li et al. (2024a) did not reveal evidence of binarity from radial velocity variations over four days in 2023, although some stars also lie above the single-star isochrone. TIC 341043961 was not observed at that time. We do not notice strong binarity signals for the g-mode pulsators in NGC 3532, as shown in Fig. 4. Evidence of close binaries can often be found in the light curves, such as eclipses or ellipsoidal variations. No such evidence was found for the majority of our cluster targets. Additionaly, tidal synchronization would generally lead to $P_{\rm spin} \approx P_{\rm orb}$. The rotation plateau identified in our sample corresponds to rotation frequencies of $f_{\rm rot} \sim 2.8$–$3.0\,{\rm d}^{-1}$, i.e. rotation periods of only ~ 0.33–0.36 days. If these stars were tidally synchronized binaries, such short rotation periods would require extremely short and identical orbital periods, which are unlikely for most stars to occur for the majority of stars in our sample without producing clear observational signatures of close binarity.

We conclude that, while binarity may account for some individual outliers (e.g., TIC 341043961) and introduce scatter in the rotation–mass diagram, it is unlikely to be the origin of the well-defined rotation plateaus observed in NGC 2516 and NGC 3532. What we observe is likely the result of genuine AM transport inside single cluster stars.

5.7. Assessing possible magnetism effects

Central magnetic fields have been detected in red giant stars with masses around $\sim 1.5\,{\rm M}_\odot$, whose progenitors could be γ Dor stars on the main sequence. The detection method is sensitive to the radial component of the field, and the inferred field strengths lie in the range of tens to hundreds of kG (Fuller et al. 2015; Stello et al. 2016a; Li et al. 2022, 2023; Deheuvels et al. 2023; Hatt et al. 2024; Villate et al. 2026). Assuming conservation of magnetic flux, the main-sequence progenitors should have central magnetic fields with strengths of several kG according to Deheuvels et al. (2023), although predictions made for observed γ Dor pulsators point to stronger fields (Aerts et al. 2021). Indeed, Takata et al. (2026) reported the detection of a central magnetic field in one γ Dor star, with a radial component consistent with the red-giant results but a much stronger azimuthal field.

It has been known for decades that magnetic fields can transport angular momentum (AM) efficiently (e.g., Spruit 2002; Fuller et al. 2019). However, following the review by Aerts et al. (2019), theoretical uncertainties remain large for current theories. Notably, the observed field strengths are several orders of magnitude higher than those predicted by a classical Tayler–Spruit dynamo. Given these inferences, we do not expect main-sequence stars to show strong differential rotation due to their internal magnetic fields. Our simplified model in Section 5.4 is therefore justified.

Regarding surface magnetic fields, Aerts (2025) suggested that weak AM loss may be operational in stars with masses up to $\sim 2.5\,{\rm M}_\odot$ due to the presence of thin convective envelopes generating small-scale dynamos, following the theory and simulations by (Rempel et al. 2023; Bekki 2025). Rather than ignoring AM loss entirely in stars more massive than $1.6\,{\rm M}_\odot$ in Section 5.4, it makes sense to allow for a tiny level of AM loss operating in this mass regime. We find that adopting an AM loss rate of $\dot{J}/J_0 \approx 0.0001\,{\rm Myr}^{-1}$ at $1.7\,{\rm M}_\odot$ allows the models to reproduce the observed rotation rates at the ages of NGC 2516 and NGC 3532, and a slightly lower AM loss rate should be applied to the $1.9\,{\rm M}_\odot$ model. Moreover, conservation of AM is also in agreement with the observational findings of a break in the specific AM at $\sim 2.5\,{\rm M}_\odot$ in Aerts (2025), as pointed out by Mombarg & Mathis (under revision). We therefore choose not to pursue a more detailed discussion of the simplified AM loss model here, as it involves too many assumptions and we only have measurements of two rotation plateaus at this stage. For this reason, we restricted our study to the AM-conservative model in Section 5.4.

As a final note we point out that there is currently no firm detection of surface magnetic fields in γ Dor stars, probably because the critical field strength required to suppress g-mode pulsations is quite small at the surface (Labadie-Bartz et al. 2025; Ballot et al. 2025; Takata et al. 2026).

6. Conclusions

In this work, we extracted and analysed g-mode period spacing patterns of member stars in NGC 3532. The membership catalogue from Pang et al. (2022) was adopted as the input list, with an additional temperature cut of $T_{\rm eff} \gtrsim 6500$ K where the slope of the main sequence shows a sharp change. We downloaded the TESS full-frame images (FFIs) and performed customised aperture photometry using the `tessutils2` pipeline, which is optimised for detecting g-mode variability. After obtaining the light curves, we computed amplitude spectra for the selected member stars and searched for g-mode period spacing patterns. For the stars showing clear patterns, we applied the TAR to measure their near-core rotation rates and asymptotic period spacings for further asteroseismic analysis.

Following the work of He et al. (2025), we used PARSEC non-rotating isochrones to determine the ages of NGC 3532 and NGC 2516. To avoid having to use uncertain rotating stellar models, we required the best-fitting isochrone to reproduce the blue edge of the observed CMD. We derived isochronal ages of

100 ± 10 Myr and 340^{+10}_{-20} Myr for NGC 2516 and NGC 3532, respectively, consistent with several previous studies.

After correcting for extinction, we plotted the CMDs of NGC 3532 and NGC 2516 for comparison. We identified an overdense region of g-mode pulsators in the lower-right corner of the CMD, which roughly corresponds to the theoretical IS of γ Dor stars. We therefore report an observational IS of young ($\lesssim$ 300 Myr) γ Dor stars, with a red edge at 7070 K and a blue edge at 7760 K. The observed instability strip overlaps with the theoretical prediction by Dupret et al. (2005) and with the distribution of γ Dor stars in the *Kepler* field (Li et al. 2020b), but it is hotter than that predicted by Bouabid et al. (2013). Beyond the blue edge, some g-mode pulsators are still found, suggesting again that multiple excitation mechanisms are responsible for driving g modes, as was previously found for older galactic γ Dor stars.

The relation between the near-core rotation rate and the stellar mass behaves distinctly below and above 1.6 $M_\odot$. Similar to NGC 2516, the stars in NGC 3532 also show an increase in near-core rotation rate with mass below 1.6 $M_\odot$. We infer that this mass marks the upper limit where magnetic braking remains effective. Above 1.6 $M_\odot$, the near-core rotation rate shows no clear dependence on mass. The high-mass stars in NGC 3532 all rotate at approximately 2.8 d^{-1}, slightly slower and with a larger spread than those in NGC 2516 ($\sim$ 3.0 d^{-1}).

We compared the evolutionary models calibrated to asteroseismology of galactic g-mode pulsators computed by Mombarg et al. (2024a) with the observed rotation rates in NGC 3532 and NGC 2516. We found that even the models with the most rapid initial rotation rates could not reproduce the observed values. We further developed simplified calculations in which the stellar rotation rate was computed from time-dependent moments of inertia derived from pre-calculated stellar structure profiles, under the assumptions of rigid rotation and angular momentum conservation. We find that the stellar models of different masses require different initial rotation rates to reproduce the observations. Furthermore, no single initial rotation rate can simultaneously account for the present-day rotation properties of both NGC 2516 and NGC 3532. This may point to a non-uniform initial rotation-rate distribution among cluster members, as recently observed in the Pleiades (Fritzewski et al. 2026). Alternatively, it may indicate that a small amount of angular momentum loss operates even in stars more massive than 1.6, $M_\odot$.

Inspection of the relation between Π_0 and stellar mass reveals some tension between the observations and current stellar models based on diffusive AM transport. For NGC 2516, the observed Π_0 values are nearly flat with mass, whereas the theoretical predictions show an increasing trend. In NGC 3532, some of the observed Π_0 values are larger than those predicted by the models. This discrepancy may indicate that current models do not yet calibrate the surface properties and core structure in a fully consistent way with the AM and chemical-element transport processes operating in these fast-rotating g-mode pulsators.

Our work on gravity-mode pulsators in open clusters highlights current limitations of 1D stellar evolution models in describing the combined effects of rotation and internal structure. In the future, more sophisticated modelling – potentially including 2D stellar structure, evolution, and pulsation models that consistently account for centrifugal distortion, rotational mixing, and angular momentum transport – may be required to resolve these discrepancies and to fully exploit the diagnostic power of asteroseismology in stellar clusters.

Acknowledgements. We thank the anonymous referee for the constructive comments and for performing a pixel-level inspection as part of the contamination check. The research leading to these results has received funding from the Flemish Government under the long-term structural Methusalem funding program by means of the project SOUL: Stellar evolution in full glory, grant METH/24/012 at KU Leuven, as well as from the European Research Council (ERC) under the Horizon Europe programme (Synergy Grant agreement N°101071505: 4D-STAR). While partially funded by the European Union, views and opinions expressed are however those of the author(s) only and do not necessarily reflect those of the European Union or the European Research Council. Neither the European Union nor the granting authority can be held responsible for them. The computational resources and services used in this work were provided by the VSC (Flemish Supercomputer Center), funded by the Research Foundation Flanders (FWO) and the Flemish Government. G.L. also acknowledges the support of the Australian Research Council through the DECRA project DE250100773, the Research Foundation Flanders (FWO) for a short stay abroad grant to attend the MESA Down Under School (grant K224824N), and travel support from the National Natural Science Foundation of China (NSFC) through grant 12273002 and the key project 12233013. C.H. also acknowledges the support of the National Natural Science Foundation of China through grant 12503045.

References

Aerts, C. 2021, Reviews of Modern Physics, 93, 015001
Aerts, C. 2025, A&A, 704, A332
Aerts, C., Augustson, K., Mathis, S., et al. 2021, A&A, 656, A121
Aerts, C., Christensen-Dalsgaard, J., & Kurtz, D. W. 2010, Asteroseismology, Springer-Verlag, Heidelberg
Aerts, C. & De Cat, P. 2003, Space Sci. Rev., 105, 453
Aerts, C., Mathis, S., & Rogers, T. M. 2019, ARA&A, 57, 35
Aerts, C., Molenberghs, G., & De Ridder, J. 2023, A&A, 672, A183
Aerts, C., Van Reeth, T., Mombarg, J. S. G., & Hey, D. 2025, A&A, 695, A214
Antoci, V., Cantiello, M., Khalack, V., et al. 2025, A&A, 696, A111
Antoci, V., Cunha, M., Houdek, G., et al. 2014, ApJ, 796, 118
Asplund, M., Grevesse, N., Sauval, A. J., & Scott, P. 2009, ARA&A, 47, 481
Ballot, J., Ihallaine, S., Ferrié, L., & Lignières, F. 2025, in TASC9/KASC16 9th TESS/16th Kepler Asteroseismic Science Consortium, 93
Balona, L. A., Joshi, S., Joshi, Y. C., & Sagar, R. 2013, MNRAS, 429, 1466
Balona, L. A., Krisciunas, K., & Cousins, A. W. J. 1994, MNRAS, 270, 905
Bastian, N., Cabrera-Ziri, I., Niederhofer, F., et al. 2017, MNRAS, 465, 4795
Bastian, N. & de Mink, S. E. 2009, MNRAS, 398, L11
Bastian, N. & Goodwin, S. P. 2006, MNRAS, 369, L9
Bastian, N., Kamann, S., Amard, L., et al. 2020, MNRAS, 495, 1978
Bedding, T. R., Murphy, S. J., Colman, I. L., & Kurtz, D. W. 2015, in European Physical Journal Web of Conferences, Vol. 101, European Physical Journal Web of Conferences, 01005
Bedding, T. R., Murphy, S. J., Crawford, C., et al. 2023, ApJ, 946, L10
Bekki, Y. 2025, A&A, 703, A262
Berry, I., Huber, D., Li, Y., et al. 2025, arXiv e-prints, arXiv:2510.20048
Beyer, A. C. & White, R. J. 2024, ApJ, 973, 28
Borucki, W. J., Koch, D., Basri, G., et al. 2010, Science, 327, 977
Bossini, D., Vallenari, A., Bragaglia, A., et al. 2019, A&A, 623, A108
Bouabid, M. P., Dupret, M. A., Salmon, S., et al. 2013, MNRAS, 429, 2500
Bouchaud, K., Domiciano de Souza, A., Rieutord, M., Reese, D. R., & Kervella, P. 2020, A&A, 633, A78
Bouma, L. G., Curtis, J. L., Hartman, J. D., Winn, J. N., & Bakos, G. Á. 2021, AJ, 162, 197
Brasseur, C. E., Phillip, C., Fleming, S. W., Mullally, S. E., & White, R. L. 2019, Astrocut: Tools for creating cutouts of TESS images, Astrophysics Source Code Library, record ascl:1905.007
Bressan, A., Marigo, P., Girardi, L., et al. 2012, MNRAS, 427, 127
Brogaard, K., Arentoft, T., Miglio, A., et al. 2023, A&A, 679, A23
Caffau, E., Ludwig, H.-G., Steffen, M., Freytag, B., & Bonifacio, P. 2011, Sol. Phys., 268, 255
Cantat-Gaudin, T., Anders, F., Castro-Ginard, A., et al. 2020, A&A, 640, A1
Cantat-Gaudin, T., Jordi, C., Vallenari, A., et al. 2018, A&A, 618, A93
Cardelli, J. A., Clayton, G. C., & Mathis, J. S. 1989, ApJ, 345, 245
Cayrel de Strobel, G., Soubiran, C., & Ralite, N. 2001, A&A, 373, 159
Çakırlı, Ö., Hoyman, B., Özdarcan, O., & Bilir, S. 2025, MNRAS, 538, 726
Che, X., Monnier, J. D., Zhao, M., et al. 2011, ApJ, 732, 68
Chen, Y., Bressan, A., Girardi, L., et al. 2015, MNRAS, 452, 1068
Choi, J., Dotter, A., Conroy, C., et al. 2016, ApJ, 823, 102
Christophe, S., Ballot, J., Ouazzani, R. M., Antoci, V., & Salmon, S. J. A. J. 2018, A&A, 618, A47
Claria, J. J. & Lapasset, E. 1988, MNRAS, 235, 1129
Claria, J. J. & Minniti, D. 1988, The Observatory, 108, 218
Clem, J. L., Landolt, A. U., Hoard, D. W., & Wachter, S. 2011, AJ, 141, 115
Cordoni, G., Milone, A. P., Marino, A. F., et al. 2018, ApJ, 869, 139
Corsaro, E., Stello, D., Huber, D., et al. 2012, ApJ, 757, 190
D'Antona, F., Di Criscienzo, M., Decressin, T., et al. 2015, MNRAS, 453, 2637

D'Antona, F., Milone, A. P., Tailo, M., et al. 2017, Nature Astronomy, 1, 0186
De Cat, P. & Aerts, C. 2002, A&A, 393, 965
Deheuvels, S., Li, G., Ballot, J., & Lignières, F. 2023, A&A, 670, L16
Dobbie, P. D., Day-Jones, A., Williams, K. A., et al. 2012, MNRAS, 423, 2815
Dotter, A. 2016, ApJS, 222, 8
Dufton, P. L., Langer, N., Dunstall, P. R., et al. 2013, A&A, 550, A109
Dupret, M. A., Grigahcène, A., Garrido, R., Gabriel, M., & Scuflaire, R. 2005, A&A, 435, 927
Eggen, O. J. 1981, ApJ, 246, 817
Espinosa Lara, F. & Rieutord, M. 2013, A&A, 552, A35
Fernandez, J. A. & Salgado, C. W. 1980, A&AS, 39, 11
Fritzewski, D. J., Barnes, S. A., James, D. J., et al. 2019, A&A, 622, A110
Fritzewski, D. J., Barnes, S. A., James, D. J., Järvinen, S. P., & Strassmeier, K. G. 2021a, A&A, 656, A103
Fritzewski, D. J., Barnes, S. A., James, D. J., & Strassmeier, K. G. 2020, A&A, 641, A51
Fritzewski, D. J., Barnes, S. A., James, D. J., & Strassmeier, K. G. 2021b, A&A, 652, A60
Fritzewski, D. J., Kemp, A., Li, G., & Aerts, C. 2026, A&A, in press, arXiv:2512.09395
Fritzewski, D. J., Van Reeth, T., Aerts, C., et al. 2024, A&A, 681, A13
Fritzewski, D. J., Vanrespaille, M., Aerts, C., et al. 2025, A&A, 698, A253
Fuller, J., Cantiello, M., Stello, D., Garcia, R. A., & Bildsten, L. 2015, Science, 350, 423
Fuller, J., Piro, A. L., & Jermyn, A. S. 2019, MNRAS, 485, 3661
Gaia Collaboration, Brown, A. G. A., Vallenari, A., et al. 2021, A&A, 649, A1
Gaia Collaboration, De Ridder, J., Ripepi, V., & Aerts, C. 2023, A&A, 674, A36
Gallet, F. & Bouvier, J. 2013, A&A, 556, A36
Garcia, S., Van Reeth, T., De Ridder, J., & Aerts, C. 2022a, A&A, 668, A137
Garcia, S., Van Reeth, T., De Ridder, J., et al. 2022b, A&A, 662, A82
Gehan, C., Mosser, B., Michel, E., Samadi, R., & Kallinger, T. 2018, A&A, 616, A24
Goupil, M. J., Dupret, M. A., Samadi, R., et al. 2005, Journal of Astrophysics and Astronomy, 26, 249
Grassitelli, L., Fossati, L., Langer, N., et al. 2015, A&A, 584, L2
Gratton, R. 2000, in Astronomical Society of the Pacific Conference Series, Vol. 198, Stellar Clusters and Associations: Convection, Rotation, and Dynamos, ed. R. Pallavicini, G. Micela, & S. Sciortino, 225
Grigahcène, A., Antoci, V., Balona, L., et al. 2010, ApJ, 713, L192
Guzik, J. A., Kaye, A. B., Bradley, P. A., Cox, A. N., & Neuforge, C. 2000, ApJ, 542, L57
Handler, G. 2009, in American Institute of Physics Conference Series, Vol. 1170, Stellar Pulsation: Challenges for Theory and Observation, ed. J. A. Guzik & P. A. Bradley, 403–409
Hastings, B., Wang, C., & Langer, N. 2020, A&A, 633, A165
Hatt, E. J., Ong, J. M. J., Nielsen, M. B., et al. 2024, MNRAS, 534, 1060
He, C., Li, C., & Li, G. 2025, ApJ, 979, 246
Heger, A., Langer, N., & Woosley, S. E. 2000, ApJ, 528, 368
Heger, A., Woosley, S. E., & Spruit, H. C. 2005, ApJ, 626, 350
Henriksen, A. I., Antoci, V., Saio, H., et al. 2023, MNRAS, 524, 4196
Hey, D. & Aerts, C. 2024, A&A, 688, A93
Hunt, E. L. & Reffert, S. 2024, A&A, 686, A42
Hurley, J. R., Tout, C. A., & Pols, O. R. 2002, MNRAS, 329, 897
Jackson, R. J., Jeffries, R. D., Wright, N. J., et al. 2022, MNRAS, 509, 1664
Johansson, K. L. V. 1981, A&AS, 43, 421
Kamann, S., Bastian, N., Gossage, S., et al. 2020, MNRAS, 492, 2177
Kamann, S., Saracino, S., Bastian, N., et al. 2023, MNRAS, 518, 1505
Kaye, A. B., Handler, G., Krisciunas, K., Poretti, E., & Zerbi, F. M. 1999, PASP, 111, 840
Keen, M. A., Bedding, T. R., Murphy, S. J., et al. 2015, MNRAS, 454, 1792
Kharchenko, N. V., Piskunov, A. E., Schilbach, E., Röser, S., & Scholz, R. D. 2013, A&A, 558, A53
Kippenhahn, R. & Weigert, A. 1990, Stellar Structure and Evolution
Koelbloed, D. 1959, Bull. Astron. Inst. Netherlands, 14, 265
Kraft, R. P. 1967, ApJ, 150, 551
Labadie-Bartz, J., Neiner, C., Ouazzani, R.-M., & Antoci, V. 2025, in TASC9/KASC16 9th TESS/16th Kepler Asteroseismic Science Consortium, 108
Lada, C. J. & Lada, E. A. 2003, ARA&A, 41, 57
Lee, U. & Saio, H. 1997, ApJ, 491, 839
Li, C., de Grijs, R., & Deng, L. 2014, Nature, 516, 367
Li, G., Aerts, C., Bedding, T. R., et al. 2024a, A&A, 686, A142
Li, G., Bedding, T. R., Murphy, S. J., et al. 2019a, MNRAS, 482, 1757
Li, G., Deheuvels, S., & Ballot, J. 2024b, A&A, 688, A184
Li, G., Deheuvels, S., Ballot, J., & Lignières, F. 2022, Nature, 610, 43
Li, G., Deheuvels, S., Li, T., Ballot, J., & Lignières, F. 2023, A&A, 680, A26
Li, G., Guo, Z., Fuller, J., et al. 2020a, MNRAS, 497, 4363
Li, G., Mombarg, J. S. G., Guo, Z., & Aerts, C. 2025, A&A, 703, A116
Li, G., Van Reeth, T., Bedding, T. R., Murphy, S. J., & Antoci, V. 2019b, MNRAS, 487, 782
Li, G., Van Reeth, T., Bedding, T. R., et al. 2020b, MNRAS, 491, 3586
Lindegren, L., Hernández, J., Bombrun, A., et al. 2018, A&A, 616, A2
Lomb, N. R. 1976, Ap&SS, 39, 447
Longmore, S. N., Kruijssen, J. M. D., Bastian, N., et al. 2014, in Protostars and Planets VI, ed. H. Beuther, R. S. Klessen, C. P. Dullemond, & T. Henning, 291–314
Luck, R. E. 1994, ApJS, 91, 309
Lurie, J. C., Vyhmeister, K., Hawley, S. L., et al. 2017, AJ, 154, 250
Mackey, A. D., Broby Nielsen, P., Ferguson, A. M. N., & Richardson, J. C. 2008, ApJ, 681, L17
Maeder, A. 2009, Physics, Formation and Evolution of Rotating Stars, Springer-Verlag, Heidelberg
Magrini, L., Viscasillas Vázquez, C., Spina, L., et al. 2023, A&A, 669, A119
Mani, P., Bedding, T. R., Bernizzoni, M., Murphy, S. J., & Hey, D. 2025, MNRAS, 542, 2866
Mankowski, C., Tayar, J., & Martin, C. 2025, arXiv e-prints, arXiv:2512.20923
Marino, A. F., Milone, A. P., Casagrande, L., et al. 2018a, ApJ, 863, L33
Marino, A. F., Przybilla, N., Milone, A. P., et al. 2018b, AJ, 156, 116
Meingast, S. & Alves, J. 2019, A&A, 621, L3
Meingast, S., Alves, J., & Rottensteiner, A. 2021, A&A, 645, A84
Meynet, G. & Maeder, A. 1997, A&A, 321, 465
Meynet, G., Mermilliod, J. C., & Maeder, A. 1993, A&AS, 98, 477
Miglio, A., Chaplin, W. J., Brogaard, K., et al. 2016, MNRAS, 461, 760
Miglio, A., Montalbán, J., Noels, A., & Eggenberger, P. 2008, MNRAS, 386, 1487
Milone, A. P., Bedin, L. R., Piotto, G., & Anderson, J. 2009, A&A, 497, 755
Milone, A. P., Marino, A. F., Di Criscienzo, M., et al. 2018, MNRAS, 477, 2640
Mombarg, J. S. G. 2023, A&A, 677, A63
Mombarg, J. S. G., Aerts, C., & Molenberghs, G. 2024a, A&A, 685, A21
Mombarg, J. S. G., Aerts, C., Van Reeth, T., & Hey, D. 2024b, A&A, 691, A131
Mombarg, J. S. G., Rieutord, M., & Espinosa Lara, F. 2023, A&A, 677, L5
Mombarg, J. S. G., Rieutord, M., & Espinosa Lara, F. 2024c, A&A, 683, A94
Mombarg, J. S. G., Van Reeth, T., & Aerts, C. 2021, A&A, 650, A58
Mowlavi, N., Barblan, F., Saesen, S., & Eyer, L. 2013, A&A, 554, A108
Mowlavi, N., Eggenberger, P., Meynet, G., et al. 2012, A&A, 541, A41
Moyano, F. D., Eggenberger, P., Salmon, S. J. A. J., Mombarg, J. S. G., & Ekström, S. 2023, A&A, 677, A6
Murphy, S. J., Bedding, T. R., Gautam, A., Kerr, R. P., & Mani, P. 2024, MNRAS, 534, 3022
Murphy, S. J., Bedding, T. R., White, T. R., et al. 2022, MNRAS, 511, 5718
Murphy, S. J., Joyce, M., Bedding, T. R., White, T. R., & Kama, M. 2021, MNRAS, 502, 1633
Netopil, M. 2017, MNRAS, 469, 3042
Netopil, M., Paunzen, E., Heiter, U., & Soubiran, C. 2016, A&A, 585, A150
Nguyen, C. T., Costa, G., Bressan, A., et al. 2025, arXiv e-prints, arXiv:2508.02393
Nguyen, C. T., Costa, G., Girardi, L., et al. 2022, A&A, 665, A126
Noyes, R. W., Hartmann, L. W., Baliunas, S. L., Duncan, D. K., & Vaughan, A. H. 1984, ApJ, 279, 763
O'Donnell, J. E. 1994, ApJ, 422, 158
Ouazzani, R. M., Marques, J. P., Goupil, M. J., et al. 2019, A&A, 626, A121
Ouazzani, R.-M., Salmon, S. J. A. J., Antoci, V., et al. 2017, MNRAS, 465, 2294
Pamyatnykh, A. A. 1999, Acta Astron., 49, 119
Pang, X., Li, Y., Yu, Z., et al. 2021, ApJ, 912, 162
Pang, X., Tang, S.-Y., Li, Y., et al. 2022, ApJ, 931, 156
Paxton, B., Bildsten, L., Dotter, A., et al. 2011, ApJS, 192, 3
Paxton, B., Cantiello, M., Arras, P., et al. 2013, ApJS, 208, 4
Pedersen, M. G. 2022, ApJ, 940, 49
Pedersen, M. G., Aerts, C., Pápics, P. I., & Rogers, T. M. 2018, A&A, 614, A128
Piatti, A. E., Claria, J. J., & Abadi, M. G. 1995, AJ, 110, 2813
Qin, S., Zhong, J., Tang, T., & Chen, L. 2023, ApJS, 265, 12
Reese, D. R., Mirouh, G. M., Espinosa Lara, F., Rieutord, M., & Putigny, B. 2021, A&A, 645, A46
Rehm, R., Mombarg, J. S. G., Aerts, C., et al. 2024, A&A, 687, A175
Rempel, M., Bhatia, T., Bellot Rubio, L., & Korpi-Lagg, M. J. 2023, Space Sci. Rev., 219, 36
Réville, V., Brun, A. S., Strugarek, A., et al. 2015, ApJ, 814, 99
Reyes, C., Stello, D., Hon, M., et al. 2024, MNRAS, 532, 2860
Reyes, C., Stello, D., Ong, J., et al. 2025, Nature, 640, 338
Ricker, G. R., Winn, J. N., Vanderspek, R., et al. 2015, Journal of Astronomical Telescopes, Instruments, and Systems, 1, 014003
Rieutord, M., Espinosa Lara, F., & Putigny, B. 2016, Journal of Computational Physics, 318, 277
Royer, F., Zorec, J., & Gómez, A. E. 2007, A&A, 463, 671
Rui, N. Z., Ong, J. M. J., & Mathis, S. 2024, MNRAS, 527, 6346
Saio, H., Bedding, T. R., Kurtz, D. W., et al. 2018a, MNRAS, 477, 2183
Saio, H., Kurtz, D. W., Murphy, S. J., Antoci, V. L., & Lee, U. 2018b, MNRAS, 474, 2774
Saio, H., Takata, M., Lee, U., Li, G., & Van Reeth, T. 2021, MNRAS, 502, 5856
Salaris, M. & Cassisi, S. 2005, Evolution of Stars and Stellar Populations

Sandquist, E. L., Stello, D., Arentoft, T., et al. 2020, AJ, 159, 96
Santos, N. C., Lovis, C., Melendez, J., et al. 2012, A&A, 538, A151
Scargle, J. D. 1982, ApJ, 263, 835
Schaller, G., Schaerer, D., Meynet, G., & Maeder, A. 1992, A&AS, 96, 269
Schmid, V. S. & Aerts, C. 2016, A&A, 592, A116
Schmid, V. S., Tkachenko, A., Aerts, C., et al. 2015, A&A, 584, A35
Scott, L. J. A. & Bowman, D. M. 2026, MNRAS, 545, staf2174
Sepulveda, A. G., Huber, D., Li, G., et al. 2023, Research Notes of the American Astronomical Society, 7, 2
Sepulveda, A. G., Huber, D., Zhang, Z., et al. 2022, ApJ, 938, 49
Spruit, H. C. 2002, A&A, 381, 923
Stello, D., Cantiello, M., Fuller, J., et al. 2016a, Nature, 529, 364
Stello, D., Vanderburg, A., Casagrande, L., et al. 2016b, ApJ, 832, 133
Sterken, C. & Jerzykiewicz, M. 1993, Space Sci. Rev., 62, 95
Sun, W., de Grijs, R., Deng, L., & Albrow, M. D. 2019a, ApJ, 876, 113
Sun, W., Duan, X.-W., Deng, L., & de Grijs, R. 2021, ApJ, 921, 145
Sun, W., Li, C., Deng, L., & de Grijs, R. 2019b, ApJ, 883, 182
Sung, H., Bessell, M. S., Lee, B.-W., & Lee, S.-G. 2002, AJ, 123, 290
Szewczuk, W. & Daszyńska-Daszkiewicz, J. 2017, MNRAS, 469, 13
Tailo, M., Corsaro, E., Miglio, A., et al. 2022, A&A, 662, L7
Takata, M., Murphy, S. J., Kurtz, D. W., Saio, H., & Shibahashi, H. 2026, MNRAS, 545, staf2153
Takata, M., Ouazzani, R.-M., Saio, H., et al. 2020a, A&A, 644, A138
Takata, M., Ouazzani, R.-M., Saio, H., et al. 2020b, A&A, 635, A106
Tayar, J. & Joyce, M. 2025, arXiv e-prints, arXiv:2502.09582
Tkachenko, A., Pavlovski, K., Johnston, C., et al. 2020, A&A, 637, A60
Townsend, R. H. D. 2003, MNRAS, 340, 1020
Townsend, R. H. D., Goldstein, J., & Zweibel, E. G. 2018, MNRAS, 475, 879
Townsend, R. H. D., Owocki, S. P., & Howarth, I. D. 2004, MNRAS, 350, 189
Townsend, R. H. D. & Teitler, S. A. 2013, MNRAS, 435, 3406
Twarog, B. A., Ashman, K. M., & Anthony-Twarog, B. J. 1997, AJ, 114, 2556
Van Reeth, T., Mombarg, J. S. G., Mathis, S., et al. 2018, A&A, 618, A24
Van Reeth, T., Tkachenko, A., & Aerts, C. 2016, A&A, 593, A120
Van Reeth, T., Tkachenko, A., Aerts, C., et al. 2015a, A&A, 574, A17
Van Reeth, T., Tkachenko, A., Aerts, C., et al. 2015b, A&A, 574, A17
Van Reeth, T., Tkachenko, A., Aerts, C., et al. 2015c, ApJS, 218, 27
Villate, M., Deheuvels, S., & Ballot, J. 2026, A&A, 707, A366
Waelkens, C. 1991, A&A, 246, 453
Wang, C., Langer, N., Schootemeijer, A., et al. 2022, Nature Astronomy, 6, 480
Wang, L., He, C., Li, C., & Li, G. 2026a, ApJ, 1000, 131
Wang, X.-Y., Wang, S., & Ong, J. M. J. 2026b, ApJ, 996, L7
Weber, E. J. & Davis, Jr., L. 1967, ApJ, 148, 217
Wright, N. J., Drake, J. J., Mamajek, E. E., & Henry, G. W. 2011, ApJ, 743, 48
Xiong, D. R., Deng, L., Zhang, C., & Wang, K. 2016, MNRAS, 457, 3163
Yang, T.-Z., Zuo, Z.-Y., Li, G., et al. 2021, A&A, 655, A63
Yuan, Z., Chang, J., Banerjee, P., et al. 2018, ApJ, 863, 26
Zahn, J.-P. 1975, A&A, 41, 329
Zhao, M., Monnier, J. D., Pedretti, E., et al. 2009, ApJ, 701, 209
Zorec, J. & Royer, F. 2012, A&A, 537, A120

Appendix A: Period spacing patterns

In this appendix, we provide a more detailed description of how we extract frequencies from the light curves and identify period-spacing patterns.

Appendix A.1: The pre-whitening algorithm

The first step is to apply a pre-whitening algorithm to the light curves, which followed a standard practice (e.g., Aerts et al. 2010, Chapter 5). In each iteration, we compute the amplitude spectrum using a Lomb–Scargle periodogram with an oversampling factor of 10 (i.e., ten frequency points per formal frequency resolution $1/T$, where T is the total time span of the observations). The frequency corresponding to the highest amplitude peak is selected. The high oversampling ensures accurate initial estimates of the frequency and amplitude. We then fit a cosine function to the light curve in the time domain, using the frequency and amplitude of the highest peak as initial guesses. The residual between the observed light curve and the best-fitting cosine model is used for the next iteration. In each iteration, the local noise level is estimated as the median amplitude within a frequency window of width $\pm 2.5\,\mathrm{d}^{-1}$ centred on each selected frequency. This relatively wide window is adopted to mitigate the impact of red noise in the low-frequency regime. As the iterations proceed and significant peaks are removed, the overall noise level decreases steadily. The pre-whitening procedure is terminated when no peak with a signal-to-noise ratio greater than four remains. As a final step, we recompute the signal-to-noise ratios of all extracted frequencies using the noise level derived from the last iteration.

Figure A.1 illustrates the step-by-step pre-whitening procedure for TIC 306045270, which we selected as a representative example from our sample. From top to bottom, the frequency with the highest amplitude is identified in each iteration. After fitting a cosine function and computing the residual, the corresponding peak is removed and no longer appears in the subsequent panels. As the pre-whitening proceeds, the noise level decreases significantly, from 1.4×10^{-4} to 2.7×10^{-5}, corresponding to a reduction by approximately a factor of five.

Appendix A.2: Period spacing pattern identification

Period spacings of g modes play an important role in probing the internal physics of stars. As noted in early studies such as Bouabid et al. (2013), Bedding et al. (2015), Van Reeth et al. (2015a), and Ouazzani et al. (2017), the period spacing ΔP varies approximately linearly with period P, which can be expressed as

$$\Delta P_i = \Sigma P_i + \Delta P_0 - \Sigma P_0, \tag{A.1}$$

where ΔP_i and P_i are the i^{th} period spacing and period, ΔP_0 and P_0 are the first period spacing and period, and Σ is the slope of the linear relation.

In practice, some periods in a g-mode series may be missing due to intrinsically low amplitudes. In such cases, period spacings cannot be computed directly. However, to avoid discarding isolated peaks, Li et al. (2019a) demonstrated that one can bypass the explicit calculation of ΔP and instead fit the linear relation directly using

$$P_i = \Delta P_0 \frac{(1+\Sigma)^i - 1}{\Sigma} + P_0. \tag{A.2}$$

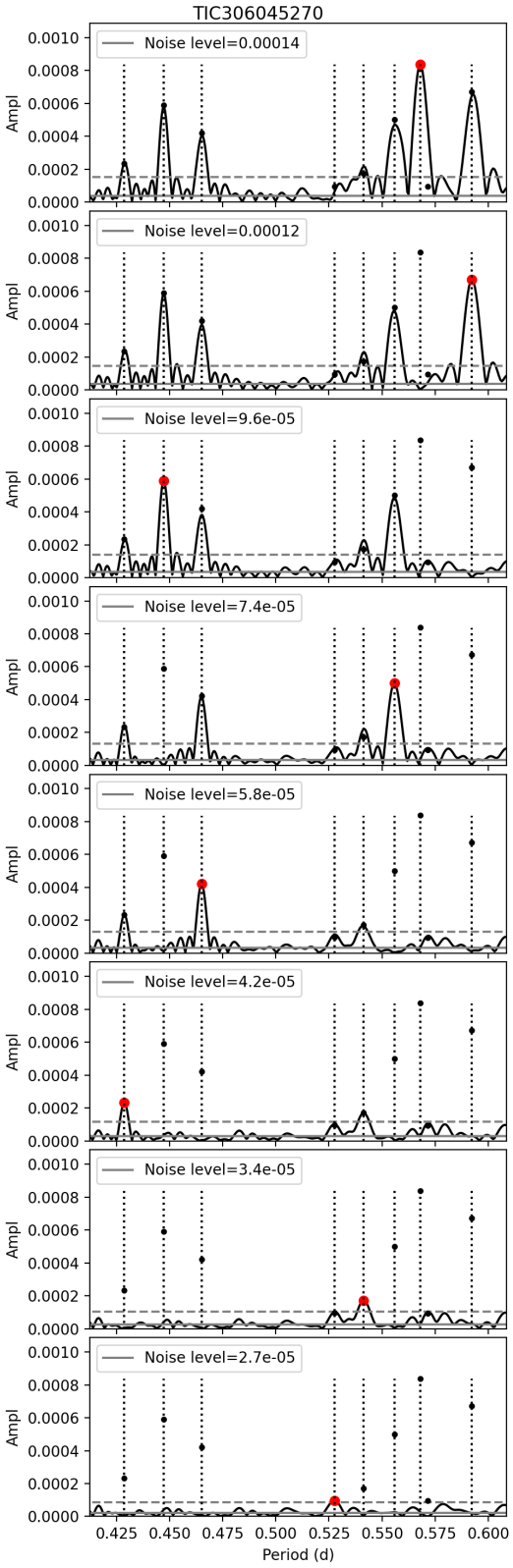

Fig. A.1. Prewhitening results for TIC 306045270. We illustrate the step-by-step extraction and removal of frequencies from top to bottom. In each panel, the black dots indicate the final set of extracted frequencies and amplitudes, while the peak extracted in that step is highlighted with a red circle. The vertical lines mark the frequencies identified as g modes in the next step. The grey horizontal line indicates the local noise level, and the horizontal dashed line shows four times this noise level.

This formulation allows the inclusion of frequencies that do not have consecutive neighbouring g-mode overtones.

Li et al. (2019a) developed a period-spacing search algorithm based on a cross-correlation function, using a g-mode template based on Eq. A.2 and the observed amplitude spectrum. They applied it to *Kepler* data of numerous γ Dor pulsators, illustrating its high performance capacity to deduce g-mode period-spacing patterns (Li et al. 2020b). In this work, we slightly modified the cross-correlation algorithm. Instead of using the multiple between a template and the amplitude spectrum, we rely on the extracted frequencies and amplitudes from the pre-whitening algorithm mentioned above. The main reason is that the Half-Height Full Width of peaks in TESS data can be in the same order of magnitude of local period spacings due to the short time span. To quantify how well a given set of template parameters reproduces the observed g-mode pattern, we define a template-matching score function $S(\Delta P_0, \Sigma)$. For a given pair of parameters $(\Delta P_0, \Sigma)$, we calculate the template period $P_k^{\rm temp}$ using Eq. A.2. Around each template period, we define a symmetric top-hat window $\mathcal{W}_k$ with a width equal to 20% of the local period spacing. This design allows the peaks to fluctuate around the linear relation, as it can be a result of chemical composition gradients (Miglio et al. 2008; Pedersen et al. 2018). The template-matching score function is defined as

$$S(\Delta P_0, \Sigma) = N_{\rm hit} \sum_{k=0}^{N_{\rm temp}-1} \sum_{i \in \mathcal{W}_k} A_i, \tag{A.3}$$

where A_i is the observed amplitude of the $i^{\rm th}$ extracted frequency, $N_{\rm temp}$ is the number of template periods considered, and $N_{\rm hit}$ denotes the number of template windows that contain at least one observed peak. The inner summation runs over all observed peaks whose period falls within the window $\mathcal{W}_k$. In this definition, $S(\Delta P_0, \Sigma)$ measures the degree of alignment between the predicted template pattern and the observed amplitude spectrum (cf. Fig. A.2). Larger values of S therefore indicate a better match between the model parameters $(\Delta P_0, \Sigma)$ and the data. By this definition, the score favours templates that encompass as many observed peaks as possible and that capture peaks with higher amplitudes.

Appendix A.3: Mode identification

Mode identification was made based on previous theoretical predictions (e.g. Van Reeth et al. 2016) and on the large *Kepler* sample presented by Li et al. (2020b), to which we refer for details. First, stellar evolution models provide prior knowledge that the asymptotic spacing Π_0 should be around ~ 4000 s, with slightly higher values expected for younger or more massive stars. Second, experience from the *Kepler* data shows that $l = 1, m = 1$ g modes are the most common and typically have the largest amplitudes. The morphology of the amplitude spectrum also helps distinguish g modes from surface modulation signals or binarity, which tend to occur at one frequency and its (sub-)harmonics, while g modes generally span a broad frequency range with multiple non-harmonic peaks. Furthermore, g-mode pulsators often form two distinct groups in the slope (Σ)–mean period ($\langle P \rangle$) plane. These properties help constrain the l and m values of the detected modes.

After identifying the period-spacing patterns and measuring the slopes, we place the g-mode pulsators in the Σ–$\langle P \rangle$ plane, as shown in Fig. A.3. Most of the stars follow the trend expected for $l = 1, m = 1$ g modes, as revealed by the *Kepler* sample.

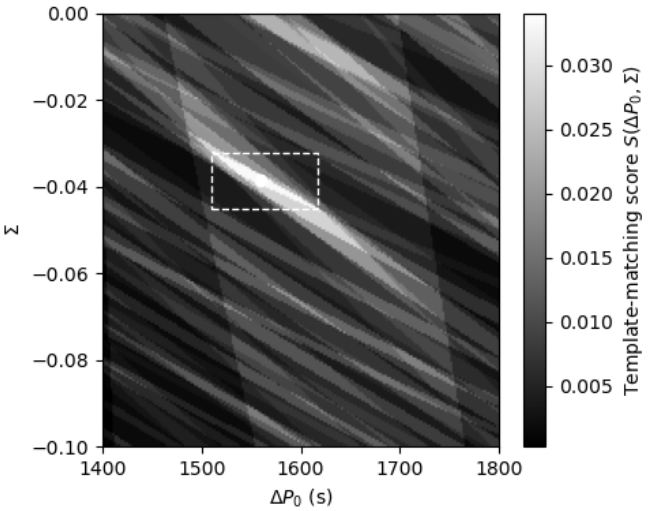

Fig. A.2. Template-matching score function $S(\Delta P_0, \Sigma)$ as a function of the first period spacing ΔP_0 and the slope Σ. We use TIC306045270 as an example. The dashed rectangle encloses the region where S exceeds 95% of its maximum value. The white point marks the centroid of this region, which we adopt as the best-fitting template.

We therefore identify these modes as $l = 1, m = 1$. The star TIC 305347034 appears to be a slight outlier. However, assuming $l = 1, m = 1$ yields a value of Π_0 consistent with theoretical expectations (see the measurement of Π_0 in the next section), whereas interpreting the modes as $l = 2, m = 2$ would double Π_0 as $\lambda \approx m^2$ when $s \gtrsim 1$ for prograde $l = m$ g modes (Saio et al. 2018a), which would be inconsistent with the star's relatively low mass inferred from its position on the CMD.

Appendix A.4: TAR fitting

There are different ways to measure the asymptotic spacing Π_0 and the near-core rotation rate $f_{\rm rot}$ using g-mode period spacings. For example, one can use the stretched échelle diagram (Christophe et al. 2018) or the linear relation between the square root of the frequency separation and the mean frequency (Takata et al. 2020b,a). In this work, we follow the methodology of Van Reeth et al. (2016).

We read the files produced by the pulsation code GYRE (Townsend & Teitler 2013; Townsend et al. 2018) to obtain the eigenvalue of the Laplace tidal equation, $\lambda_{l,m,s}$, which is a function of l, m, and the spin parameter $s = 2f_{\rm rot}/f_{nlm,{\rm co}}$. Here $f_{nlm,{\rm co}}$ is the g-mode pulsation frequency in the co-rotating frame. The g-mode periods in the co-rotating frame are calculated as

$$P_{nlm,{\rm co}} = \frac{1}{f_{nlm,{\rm co}}} = \frac{\Pi_0}{\sqrt{\lambda_{l,m,s}}} \left(n + \alpha_{\rm g}\right), \tag{A.4}$$

where n is the radial order and $\alpha_{\rm g}$ is a phase term, which we fix at 0.5. Since $f_{nlm,{\rm co}}$ appears on both sides of the equation, we rearrange Eq. A.4 and multiply both sides by $2f_{\rm rot}$ to obtain

$$s\sqrt{\lambda_{l,m,s}} = 2\Pi_0 f_{\rm rot}\left(n + \alpha_{\rm g}\right). \tag{A.5}$$

Equation A.5 can be used to solve for $P_{nlm,{\rm co}}$ for given values of Π_0, $f_{\rm rot}$, and n. The transformation to the inertial frame is then given by

$$P_{nlm,{\rm in}} = \frac{1}{f_{nlm,{\rm co}} + m f_{\rm rot}}. \tag{A.6}$$

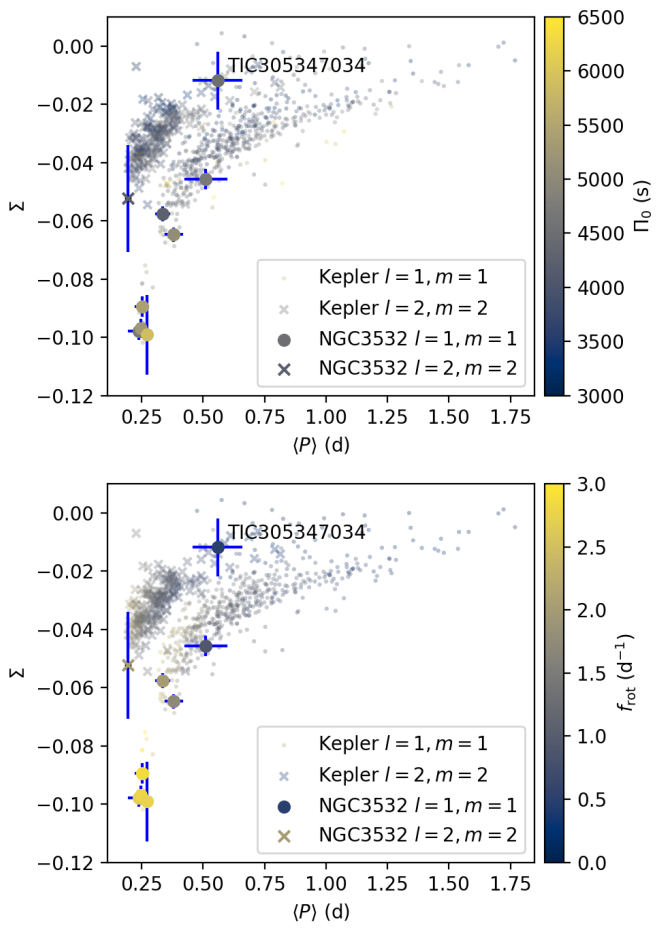

Fig. A.3. Slope Σ as a function of the mean period ⟨*P*⟩ for g-mode pulsators from the *Kepler* field reported by Li et al. (2020b) and from this work. The horizontal bars indicate the range between the minimum and maximum periods, rather than the uncertainty in ⟨*P*⟩. Top panel: colour-coded by the asymptotic spacing Π_0; bottom panel: by the near-core rotation rate $f_{\rm rot}$.

In the fitting procedure, we do not require the model periods to match the observed periods exactly. This is because the phase term $\alpha_{\rm g}$ is fixed and additional physical effects that may influence the period values are not included in our modelling, such as chemical gradients (Miglio et al. 2008). Instead, we interpolate the theoretically calculated period spacings and fit the observed period spacings. The optimisation of Π_0 and $f_{\rm rot}$ is performed using a standard Markov Chain Monte Carlo (MCMC) approach based on minimising χ^2 residuals, i.e. maximising a Gaussian likelihood. We do not adopt the formal observational uncertainties of the period spacings, as they are typically very small and do not reflect the dominant sources of uncertainty, such as deviations from the asymptotic relation. Instead, we use the residuals between the observed period spacings and their best-fitting linear relation as the uncertainties. This allows us to account for systematic deviations from the asymptotic relation. As discussed above, period-spacing patterns can still be identified even when the periods are not strictly consecutive. If a period-spacing sequence contains four or fewer spacings, we instead use the period spacings predicted by the linear relation as input. In such cases, the frequency resolution is adopted as the uncertainty.

Figure A.4 displays all g-mode pulsators with clear period-spacing patterns identified in this work, sorted by descending brightness from top to bottom. The red vertical lines mark the near-core rotation period ($1/f_{\rm rot}$). The locations of $l = 1, m = 1$ g modes are indicated for each star, together with the possible locations of $l = 2, m = 2$ g modes. Figure A.5 displays the amplitude spectra up to $72\,{\rm d}^{-1}$, allowing us to inspect their p-mode pulsations. We find that TIC 306384085, TIC 305909136, and TIC 306503983 show hybrid pulsations.

We also considered the possibility that nonlinear combinations of p-mode frequencies may fall in the g-mode frequency range. We checked for such combination frequencies following the procedure described in Sect. 4.1 of Li et al. (2019a). In brief, for each star, we selected two parent frequencies, f_1 and f_2, from the 20 highest-amplitude frequencies and examined low-order combinations of the form $n_1 f_1 + n_2 f_2$, with integer coefficients satisfying $|n_1| + |n_2| \leq 2$. A frequency f was considered a possible combination frequency when $|f - (n_1 f_1 + n_2 f_2)| < \epsilon$. For *Kepler* data, Li et al. (2019a) adopted $\epsilon_0 = 0.0002\,{\rm d}^{-1}$. For the TESS light curves used here, we scaled this tolerance according to the time span T of the light curve, adopting $\epsilon = \epsilon_0(4\,{\rm yr}/T)$. We found no strong evidence that our g-mode period-spacing patterns are contaminated by combination frequencies. We therefore conclude that p-mode combination frequencies do not affect the period-spacing patterns analysed in this work.

Appendix A.5: Period spacing patterns of our sample

We present all the period spacing patterns identified from the g-mode pulsators in NGC 3532, from Fig. A.6 to Fig. A.12.

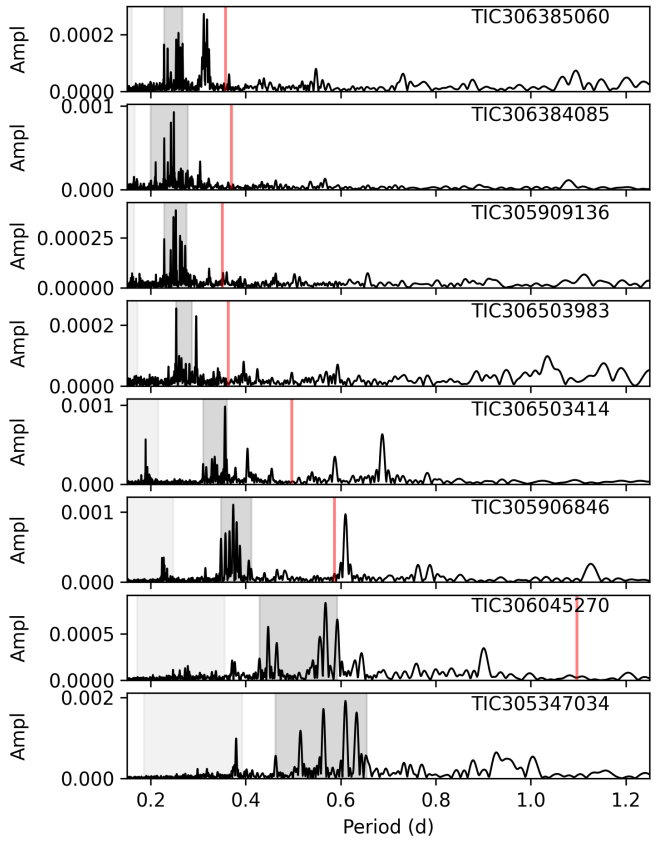

Fig. A.4. Amplitude spectra of all the g-mode pulsators in NGC 3532, sorted by their G-band magnitude, with brighter stars shown at the top and fainter stars at the bottom. The dark grey regions mark the locations of $l = 1$ g modes, while the light grey regions indicate the predicted locations of $l = 2$ g modes, spanning from 0.4 times the minimum period to 0.6 times the maximum period of the $l = 1$ g modes. The vertical red lines show the near-core rotation frequencies measured using the TAR. There is no vertical red line in the bottom panel because the rotation rate is out of the x-axis range.

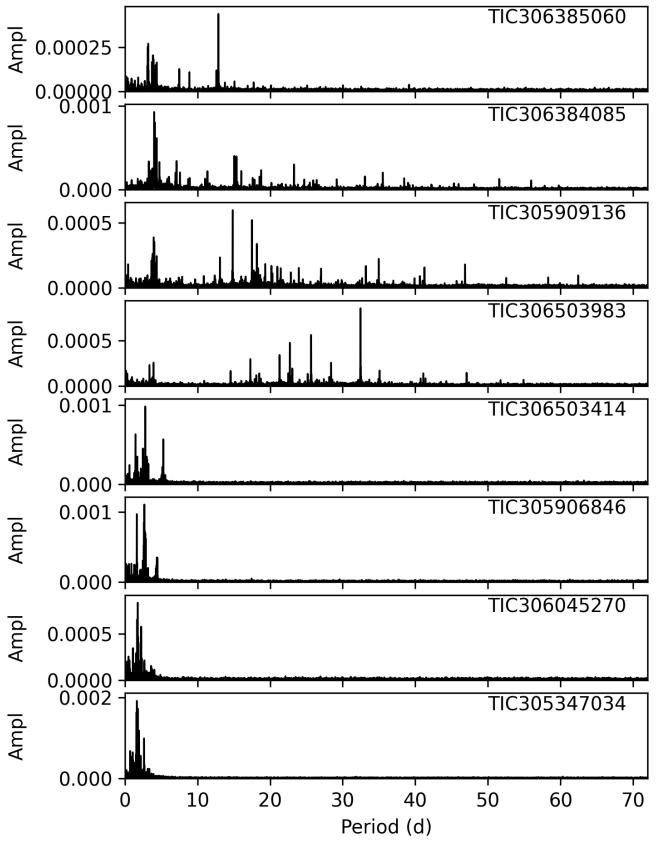

Fig. A.5. Same as Fig. A.4, but showing the full frequency range.

Table A.1. Gravity-mode periods of TIC305347034.

(n, l, m)	P (d)
(14,1,1)	0.46286(9)
(16,1,1)	0.51495(6)
(18,1,1)	0.56389(5)
(19,1,1)	0.5864(6)
(20,1,1)	0.60996(5)
(21,1,1)	0.63273(7)
(22,1,1)	0.65461(22)

Table A.2. Gravity-mode periods of TIC305906846.

(n, l, m)	P (d)
(15,1,1)	0.34825(4)
(16,1,1)	0.35749(4)
(17,1,1)	0.36577(3)
(18,1,1)	0.373783(24)
(19,1,1)	0.38112(3)
(20,1,1)	0.38801(6)
(23,1,1)	0.40676(11)
(24,1,1)	0.41211(18)

Table A.3. Gravity-mode periods of TIC305909136.

(n, l, m)	P (d)
(11,1,1)	0.228476(29)
(13,1,1)	0.24219(4)
(14,1,1)	0.247913(23)
(15,1,1)	0.252929(22)
(17,1,1)	0.26188(4)
(18,1,1)	0.26563(5)
(19,1,1)	0.2693(10)
(20,1,1)	0.27257(5)
(21,1,1)	0.27542(12)

Table A.4. Gravity-mode periods of TIC306045270.

(n, l, m)	P (d)
(15,1,1)	0.42875(13)
(16,1,1)	0.44728(6)
(17,1,1)	0.46510(8)
(21,1,1)	0.5276(5)
(22,1,1)	0.54133(28)
(23,1,1)	0.5558(10)
(24,1,1)	0.56794(6)
(26,1,1)	0.59227(9)

Table A.5. Gravity-mode periods of TIC306384085.

(n, l, m)	P (d)
(8,1,1)	0.20012(5)
(9,1,1)	0.210447(18)
(11,1,1)	0.228545(12)
(12,1,1)	0.236045(28)
(13,1,1)	0.242683(11)
(14,1,1)	0.24872(10)
(16,1,1)	0.25906(5)
(17,1,1)	0.26345(4)
(18,1,1)	0.26732(4)
(20,1,1)	0.27455(6)
(21,1,1)	0.27777(5)

Table A.6. Gravity-mode periods of TIC306385060.

(n, l, m)	P (d)
(11,1,1)	0.228181(27)
(12,1,1)	0.23567(3)
(13,1,1)	0.24232(7)
(15,1,1)	0.25368(3)
(16,1,1)	0.258467(28)
(17,1,1)	0.26290(4)
(18,1,1)	0.26711(4)

Table A.7. Gravity-mode periods of TIC306503414. This star has two period-spacing patterns with $l = 1$ and $l = 2$, respectively.

(n, l, m)	P (d)
(18,1,1)	0.31038(6)
(19,1,1)	0.31698(7)
(21,1,1)	0.32906(5)
(22,1,1)	0.33460(5)
(23,1,1)	0.33947(14)
(27,1,1)	0.356501(21)
(28,1,1)	0.36047(18)
(33,2,2)	0.189355(8)
(35,2,2)	0.19194(4)
(36,2,2)	0.193073(25)
(38,2,2)	0.19523(5)
(39,2,2)	0.19644(7)
(40,2,2)	0.19727(4)

Table A.8. Gravity-mode periods of TIC306503983.

(n, l, m)	P (d)
(13,1,1)	0.253777(25)
(14,1,1)	0.25964(7)
(15,1,1)	0.26490(8)
(17,1,1)	0.27394(9)
(19,1,1)	0.28134(12)
(20,1,1)	0.28394(15)
(21,1,1)	0.28723(16)

Appendix B: The dominant frequency as a tool to estimate the near-core rotation rate

Gravity modes do not necessarily exhibit clear period-spacing patterns. Instead, for several reasons – such as short light curves or missing modes – g-mode pulsations may sometimes appear only as a single amplitude hump in the low-frequency regime, particularly for short time series photometry. Owing to the transformation from the co-rotating frame to the inertial frame ($+mf_{\rm rot}$, where m is the azimuthal order and $f_{\rm rot}$ is the rotation rate), the location of the mean or dominant frequency $f_{\rm dom}$ within the amplitude hump is strongly correlated with the rotation rate. Therefore, $f_{\rm dom}$ can be used to estimate the near-core rotation rate. This method obviously exhibits a larger scatter and systematic deviations compared to period-spacing analyses, but it can be applied to a much larger number of stars. Sepulveda et al. (2022) and Sepulveda et al. (2023) applied this method to two exoplanet host stars and measured their rotation rates and inclinations. Aerts et al. (2025) tested this technique on *Gaia* light curves of 105 well-known *Kepler* pulsators with a carefully identified dominant prograde dipole mode in the gravito-inertial regime. This allowed them to come up with the following regression formula to estimate the near-core rotation frequency, provided that the dominant mode has dipole prograde geometry and an amplitude above 4 ppt:

$$f_{\rm rot} = 0.836^{+0.023}_{-0.027} f_{\rm dom} - 0.272^{+0.041}_{-0.036}\,{\rm d}^{-1}, \tag{B.1}$$

where the estimated value of $f_{\rm rot}$ has an uncertainty between $+0.123\,{\rm d}^{-1}$ and $-0.164\,{\rm d}^{-1}$. This regression formula was subsequently used to estimate the near-core rotation rates for approximately 2500 galactic g-mode pulsators to demonstrate how stellar rotation near the convective core slows down with evolution (Aerts 2025). This regression was also applied to the g-mode pulsators to study the rotational evolution of stars in the Pleiades (Fritzewski et al. 2026).

To test the robustness of Eq. B.1, we selected the $f_{\rm dom}$ values of the eight g-mode pulsators with clear period spacings and compared the near-core rotation rates derived from both Eq. B.1 and the TAR. As shown in Fig. B.1, we find that the two methods are generally consistent. It seems that the stars with slower rotations ($f_{\rm rot} < 1.0\,{\rm d}^{-1}$) exhibit larger discrepancies. This is because, in the slow-rotation regime, the frame transformation term $+mf_{\rm rot}$ is no longer dominant. Instead, other factors, such as the radial orders at which the modes are excited and the mode amplitudes, which do not follow a simple pattern, may lead to deviations. For the fast rotators, the results are generally consistent within $\pm 2\sigma$.

Going back to Fig. A.4 we can understand why the real data lead to scatter in the simplified linear approximation of Eq. B.1. The top star, TIC 306385060, shows unresolved g modes outside the grey region where the resolved g modes are located, and there is a gap where the g-mode amplitudes are small. If we use this unresolved peak as $f_{\rm dom}$, we will obtain a large deviation from Eq. B.1. The same situation appears in TIC 306503983, TIC 306503414, and TIC 306045270, whose dominant peaks are not located near the middle of the g-mode patterns. Despite the occurring deviations, the simple linear prediction formula in Eq. B.1 gives a meaningful estimate of the near-core rotation frequency for stars without any g-mode pattern, requiring only the dominant frequency as input.

After verifying the performance of Eq. B.1 on stars with known near-core rotation rates, we apply this relation to a larger sample of g-mode pulsators in NGC 3532. We measured the dominant frequencies of the g-mode pulsators in NGC 3532 and plotted the inferred $f_{\rm rot}$ values from Eq. B.1 in the left panel of Fig. B.2. We also plot the stars whose near-core rotation rates were measured from a period spacing pattern with the TAR as a benchmark. We find that for masses below $\sim 1.6\,{\rm M}_\odot$, most stars overlap with those showing clear period-spacing patterns, indicating that interpreting the dominant frequencies as $l = 1$ prograde g modes is tenable. However, we identify another group of stars with $M \lesssim 1.6\,{\rm M}_\odot$ that is clearly separated from the primary sequence of points; these stars are enclosed by the yellow region (Region 1). We tested several alternative mode identifications, including surface modulation, $l = 2$ prograde g modes, and retrograde Rossby modes. We find that classifying their dominant frequencies as a prograde $l = 2$ g mode reproduces the $f_{\rm rot}$–mass relation seen in the other stars, as shown by the black circles in the middle panel of Fig. B.2.

We also identified another group of stars in the left panel of Fig. B.2, enclosed by the green region (Region 2), with masses spanning 1.7–1.9 $\,{\rm M}_\odot$. As shown in the middle panel of Fig. B.2, interpreting the dominant frequency of these stars as surface-modulation signal yields rotation rates consistent with those of stars exhibiting clear period-spacing patterns and extends the plateau at $\sim 2.8\,{\rm d}^{-1}$ to $1.9\,{\rm M}_\odot$. The presence of more stars with surface modulations at the high-mass end is also consistent with the results found for NGC 2516 (Li et al. 2024a).

We also notice several outliers that are difficult to explain. We identify four stars whose rotation rates reach $3.3\,{\rm d}^{-1}$, calculated by assuming that their dominant frequencies correspond to $l = 1$ g modes. These rotation rates are even higher than those of the most rapidly rotating stars in NGC 2516, whose age is only about one half to one third that of NGC 3532. If these signals are interpreted as surface modulations, the inferred rotation rates would be even higher ($\sim 4.3\,{\rm d}^{-1}$). Alternatively, if they are identified as $l = 2$ g modes, the resulting rotation rates would be $\sim 1.5\,{\rm d}^{-1}$.

In addition, there are several slow rotators with masses between 1.7 and $2.0\,{\rm M}_\odot$. If these signals are genuine, they may have undergone some braking processes, such as star–disc interaction (Bastian et al. 2020), binary mergers (Wang et al. 2022), or tidal locking (D'Antona et al. 2015, 2017). However, as shown in the right panel of Fig. B.2, we find that these stars typically suffer from severe contamination by nearby stars. Their dominant frequencies may therefore simply be polluted signals. We also clarify that a severely contaminated star does not necessarily show extra low-frequency peaks if the nearby star is quiet.

Overall, the middle and right panels of Fig. B.2 reinforce the results on the rotation rates presented and discussed in the main manuscript. The extra stars discussed and displayed here may be interesting targets to revisit when TESS observations during more than two consecutive sectors become available.

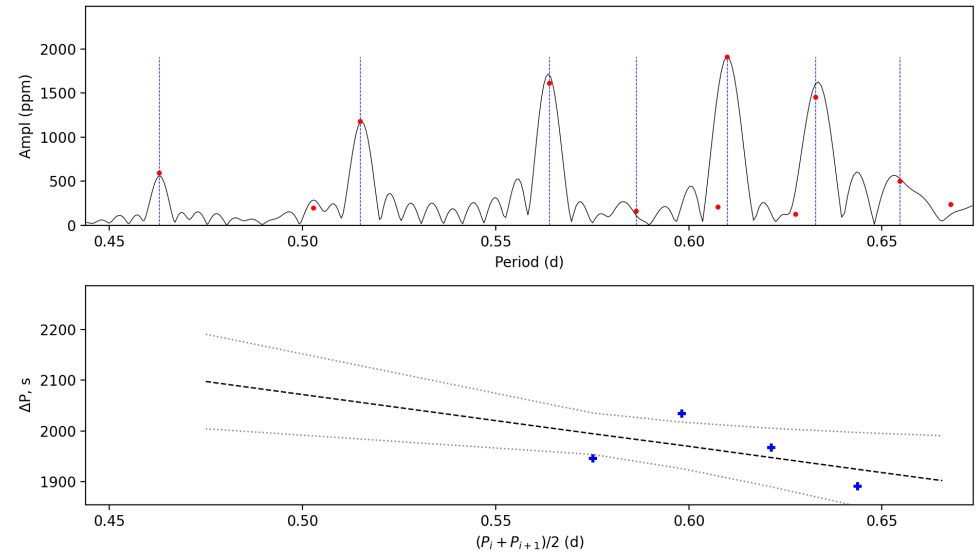

.

Fig. A.6. Same as Fig. 1 for TIC 305347034.

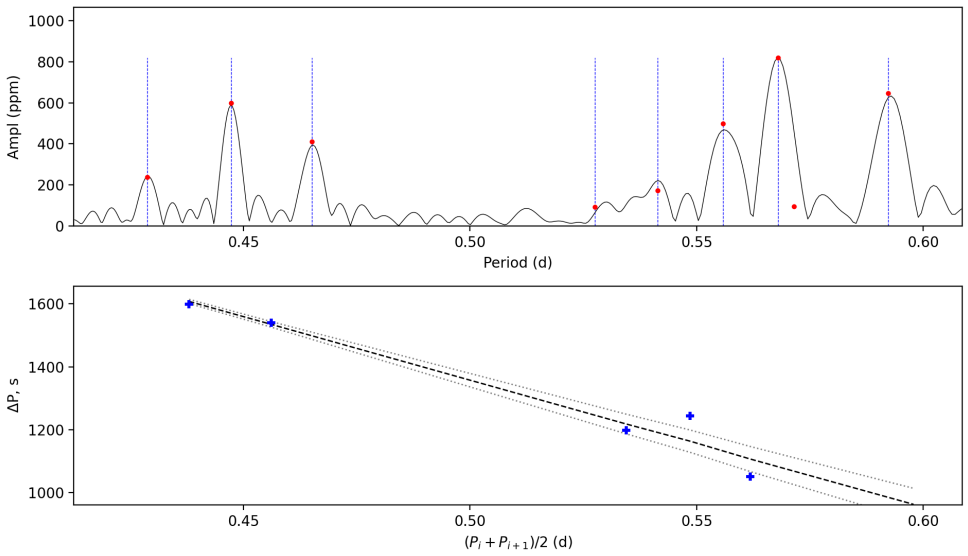

Fig. A.7. Same as Fig. 1 for TIC 306045270.

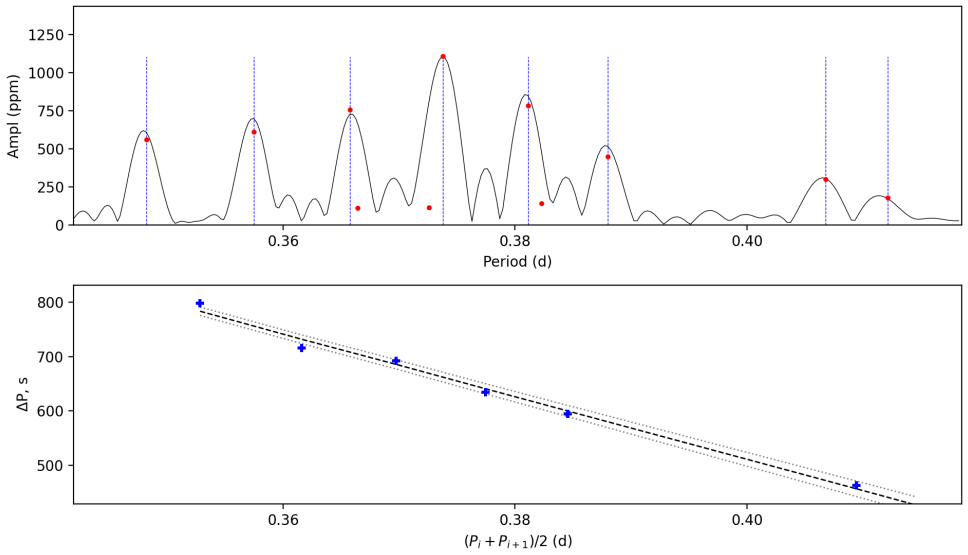

Fig. A.8. Same as Fig. 1 for TIC 305906846.

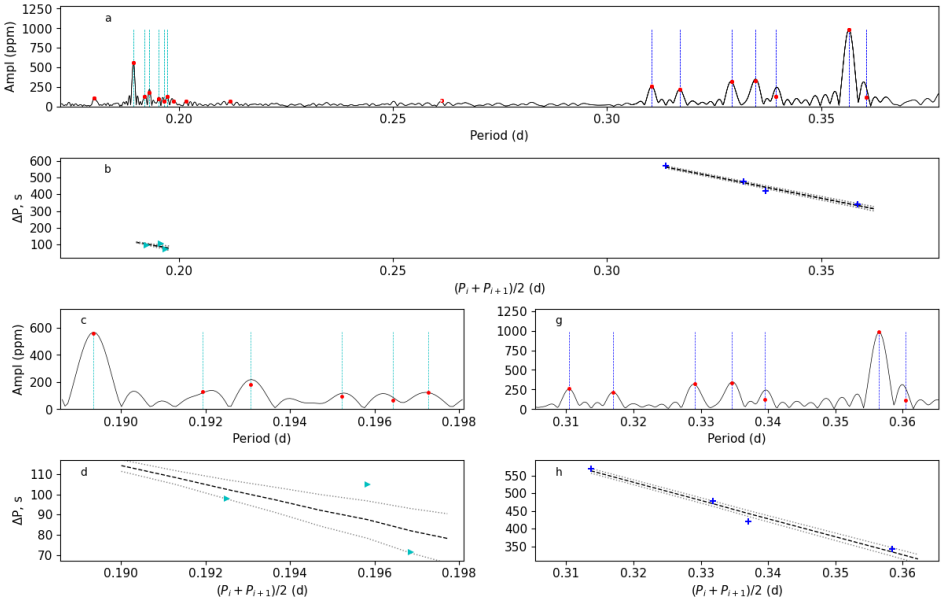

Fig. A.9. Panels a and b are the same as Fig. 1 for TIC 306503414. Panels c and d zoom in on the $l = 2, m = 2$ g modes, while panels g and h zoom in on the $l = 1, m = 1$ g modes.

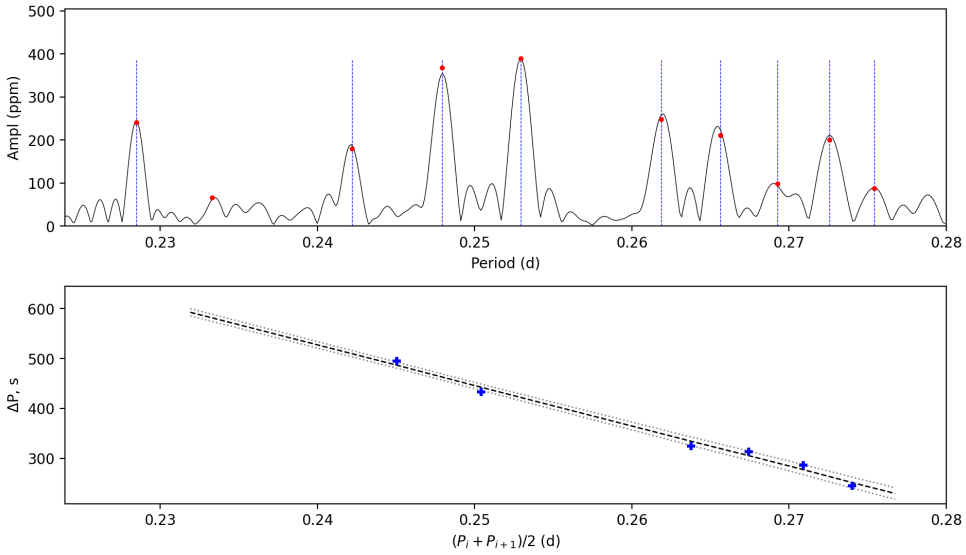

Fig. A.10. Same as Fig. 1 for TIC 305909136.

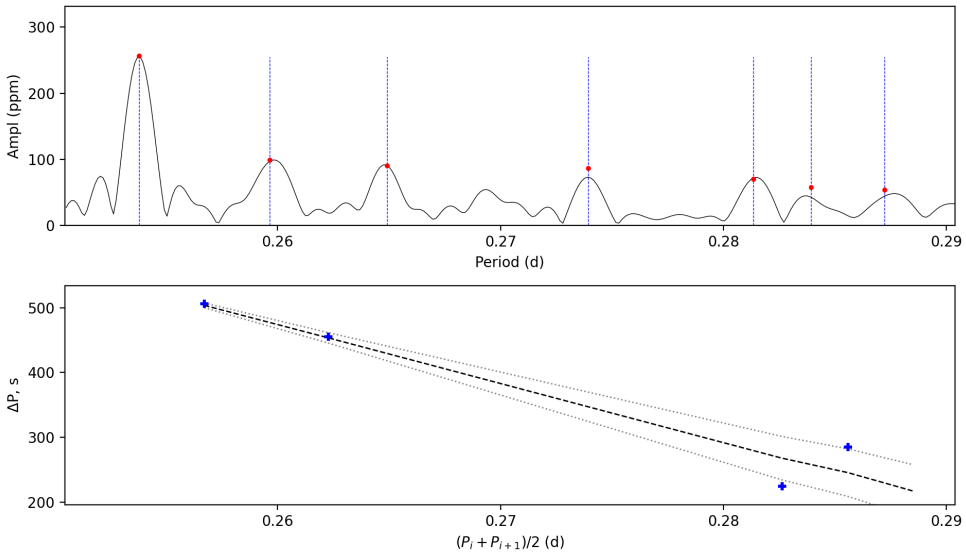

Fig. A.11. Same as Fig. 1 for TIC 306503983.

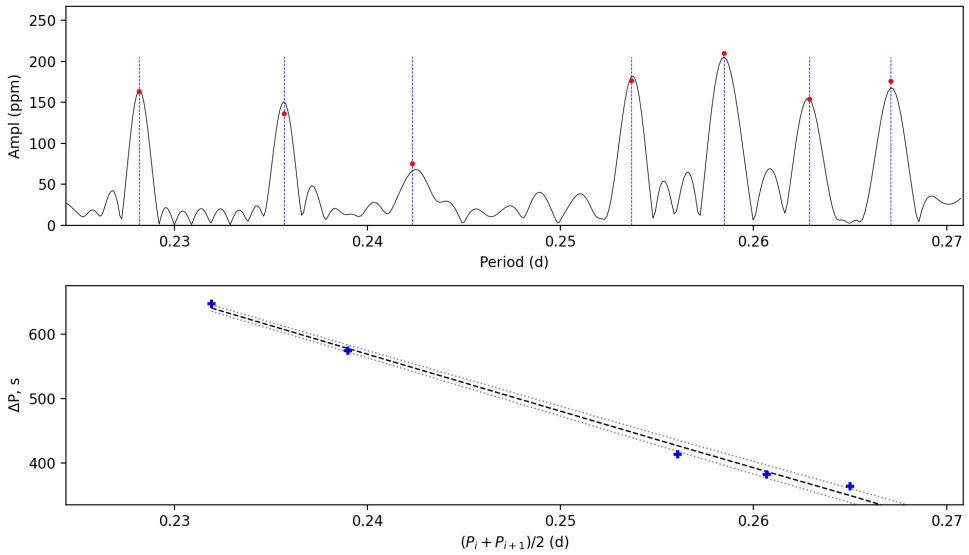

Fig. A.12. Same as Fig. 1 for TIC 306385060.

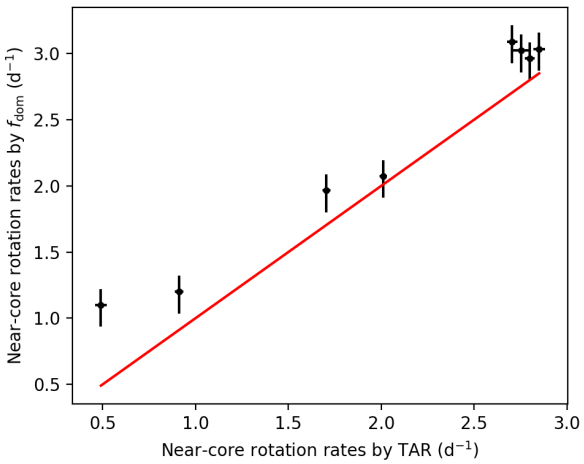

Fig. B.1. Near-core rotation rates calculated by Eq. B.1 and by the TAR. The red line shows the 1:1 relation.

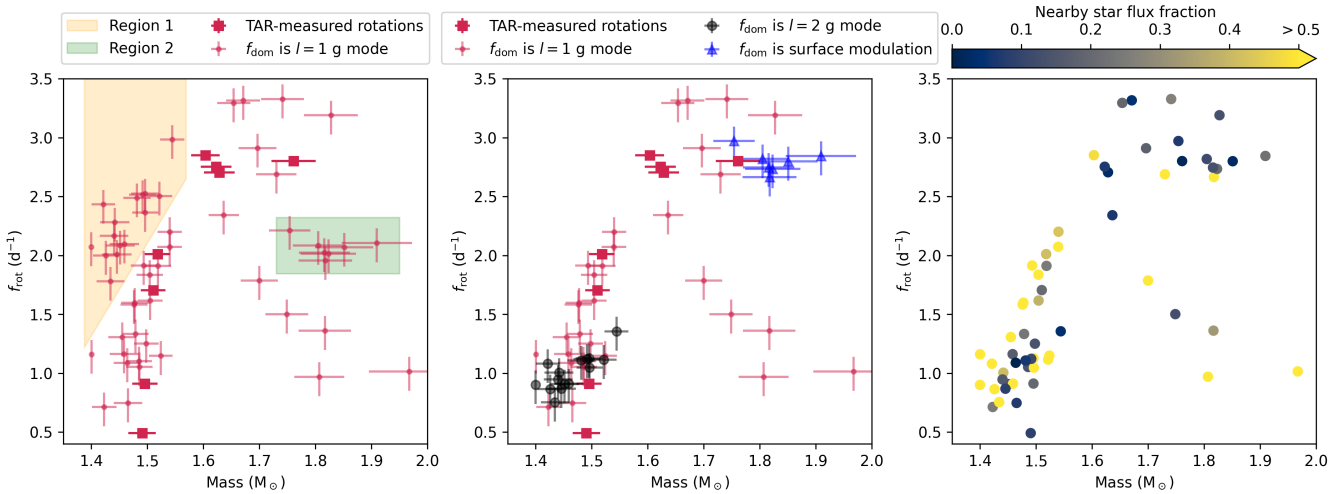

Fig. B.2. Additional near-core or surface rotation rates inferred from dominant frequencies in the g-mode frequency regime of stars in NGC 3532. *Left panel:* Near-core rotation rate measured either from TAR fitting (red squares) or by assuming that the dominant frequency corresponds to an $l = 1$ prograde g mode (red dots). Two regions with potentially ambiguous mode identifications are highlighted: Region 1 at the lower-mass end and Region 2 at the higher-mass end. *Middle panel:* Rotation rates after revising the mode identification of the dominant frequency. Black circles indicate stars whose dominant frequency is more consistent with an $l = 2$ prograde g mode, while blue triangles denote stars whose dominant frequency is likely caused by surface modulation. *Right panel:* Same as the middle panel, but colour-coded by the contamination level, quantified by the flux fraction contributed by nearby stars.